JOURNAL OF GEOPHYSICAL RESEARCH, VOL. 112, B03403, doi:10.1029/2006JB004344, 2007

Ground motion measurement in the Lake Mead area, Nevada, by differential synthetic aperture radar interferometry time series analysis: Probing the lithosphere rheological structure

O. Cavalié,[1] M.-P. Doin,[1] C. Lasserre,[1] and P. Briole[2]

Received 13 February 2006; revised 28 July 2006; accepted 13 October 2006; published 13 March 2007.

[1] We measure ground motion around the Lake Mead, Nevada, using synthetic aperture radar interferometry. The lake water level has fluctuated through time since impoundment in 1935. To quantify the deformation due to water level variations over the past decade, and to constrain the crust and mantle rheological parameters in the lake area, we analyze 241 interferograms based on 43 ERS images acquired between 1992 and 2002. All interferograms have a high coherence due to arid conditions. Most of them show strong atmospheric artefacts. Tropospheric phase delays are estimated and corrected for each interferogram by analyzing the phase/elevation correlation. Corrections are validated using data from the ERA40 global atmospheric reanalysis. Corrected interferograms are inverted pixel by pixel to solve for the time series of ground motion in the lake area. Temporal smoothing is added to reduce random atmospheric artefacts. The observed deformation is nonlinear in time and spreads over a 50×50 km^2 area. We observe a 16 mm subsidence between 1995 and 1998 due to an 11 m water level increase, followed by an uplift due to the water level drop after 2000. We model the deformation, taking into account the loading history of the lake since 1935. A simple elastic model with parameters constrained by seismic wave velocities does not explain the amplitude of the observed motion. The two-layer viscoelastic model proposed by Kaufmann and Amelung (2000), with a mantle viscosity of 10^{18} Pa s, adjusts well the data amplitude and its spatiotemporal shape.

Citation: Cavalié, O., M.-P. Doin, C. Lasserre, and P. Briole (2007), Ground motion measurement in the Lake Mead area, Nevada, by differential synthetic aperture radar interferometry time series analysis: Probing the lithosphere rheological structure, *J. Geophys. Res.*, *112*, B03403, doi:10.1029/2006JB004344.

1. Introduction

[2] This study investigates whether the transient, nonelastic, deformation of the lithosphere in response to a load can be measured on a decade timescale. We focus on the area of the Lake Mead, an important water reservoir in Nevada (Figure 1). Sedimentation in the lake and water level fluctuations since the lake impoundment in 1935 act as a varying load on the lithosphere. They induce ground deformation, expected to be mainly controlled by the crust and upper mantle rheological properties. We use synthetic aperture radar interferometry (InSAR) to accurately measure this deformation through space and time between 1992 and 2002. As the loading function is well known, this study gives a unique opportunity to constrain the lithosphere rheology in the Lake Mead area, in the central Basin and Range province.

[3] The accurate knowledge of the crust and mantle rheology is an important scientific issue. Crust bending under topographical loads, postglacial rebound or postseismic deformation have long been used as probes of crust and mantle rheology. However, the sensitivity of these studies to the mantle rheological structure is highly dependent on the length and timescales of the observed deformation. Global postglacial rebound studies constrain the lithosphere thickness, the upper mantle, and top lower mantle viscosity. They lead to an elastic plate thickness of 80 to 120 km and an average mantle viscosity of about 10^{21} Pa s [*Peltier*, 1984], possibly differentiated into a 4×10^{20} Pa s upper mantle and a 10^{22} Pa s lower mantle [*Lambeck et al.*, 1998]. However, they are biased toward shield rheological structure, because large ice caps were mainly located on cratons. Rebound studies around smaller ice caps (British islands, [*Lambeck et al.*, 1996]) or former lakes (Bonneville [*Nakiboglu and Lambeck*, 1983]) yield additional constraints on the local rheological structure of the uppermost mantle. They show that the upper mantle viscosity is lower away from shields

[1] Laboratoire de Géologie, École Normale Supérieure, CNRS, Paris, France.
[2] Institut de Physique du Globe de Paris, Centre National de la Recherche Scientifique, Paris, France.

0148-0227/07/2006JB004344$09.00

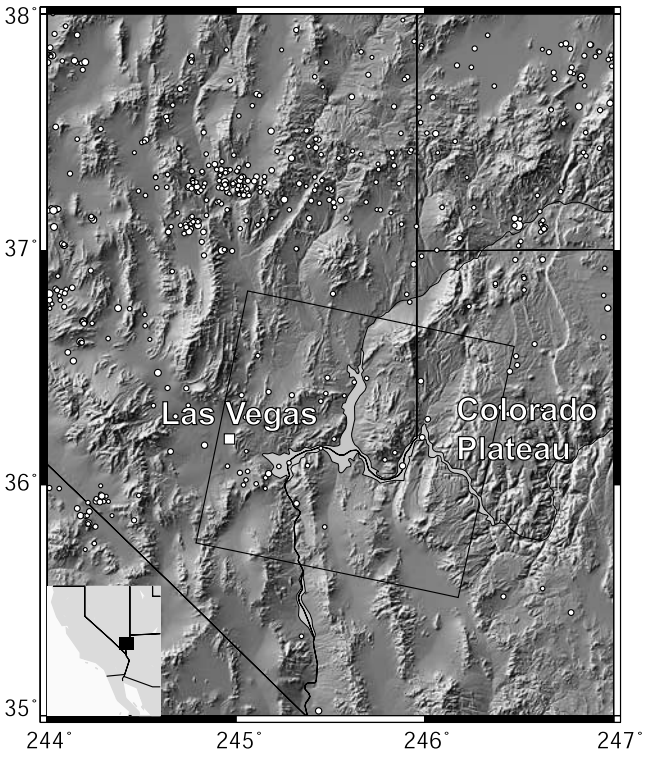

Figure 1. Shaded relief topographic map of Lake Mead area from 3-arc sec Shuttle Radar Topography Mission (SRTM) digital elevation model (DEM). Black rectangle shows the location of descending radar scenes. White circles are epicenters of regional earthquakes ($2.5 \leq M_w \leq 4$) for the period 1992–2002. Locations and magnitudes are from Advanced National Seismic System (ANSS) catalog.

than below them. The mantle viscous behavior might also change with the observation time scale. It has been argued that the moderate viscosity inferred from postglacial rebound for the cratonic lithospheric roots (on timescales <10,000 years) is at odds with their long-term stability (>1.6 Gyr), suggesting possible transient rheology [*Fleitout et al.*, 2005]. Recently, geodetic studies of postseismic deformations following large earthquakes have been interpreted in terms of crust and mantle rheology at timescales of a few days to decades [e.g., *Pollitz et al.*, 2000]. They provide lower estimates of the elastic thickness and of the viscosity in the lower crust and upper mantle than those derived from postglacial rebound. In the Central Nevada Seismic Belt (western United States), postseismic relaxation events are explained by a low viscosity in the lower crust ($\sim 10^{19}$ Pa s [*Hetland and Hager*, 2003]) or in the upper mantle ($\sim 10^{18}$ Pa s, [*Gourmelen and Amelung*, 2005]). In the northern Basin and Range province, *Nishimura and Thatcher* [2003] argue from the relaxation of the 1959, M_w = 7.3, Hebgen Lake earthquake that the elastic plate thickness is close to 38 km and that the underlying viscoelastic asthenosphere has a viscosity of 4×10^{18} Pa s.

[4] In the Lake Mead area (Figure 1), water loading after lake impoundment induced a ground subsidence that nearly stopped after a small relaxation time (≤25 years [*Lara and Sanders*, 1970]). *Kaufmann and Amelung* [2000] used levelling data showing a subsidence of up to 17 cm between 1935 and 1950 [*Longwell*, 1960], to derive an elastic thickness of 30 km and a viscosity of the underlying upper mantle of the order of 10^{18} Pa s. Although the load is known with accuracy, uncertainties in their study arise from the limited accuracy of subsidence measurement using levelling methods.

[5] Here, we focus on the 1992–2002 period, during which the water level in the lake varies by almost 15 m, with an increase from 1992 to 1998, followed by a drop since 2000 (Figure 2). Using the rheological parameters inverted by *Kaufmann and Amelung* [2000], the complete lake level history since 1935, and a progressive sediment loading, the expected relative subsidence over a distance of 50 km is of up to 1.5 cm between 1992 and 1998, corresponding to a subsidence spatial gradient of 3×10^{-7}. The purpose of this work is first to demonstrate that InSAR can accurately measure the temporal evolution of such a small centimetric deformation on a 50-km-wide spatial scale. The deformation measurements are then used to discuss the rheological parameters of the crust and upper mantle in the Lake Mead area.

[6] SAR interferometry is widely used for monitoring ground motions. The subsidence measurement by InSAR requires the reflected phase of the electromagnetic wave to

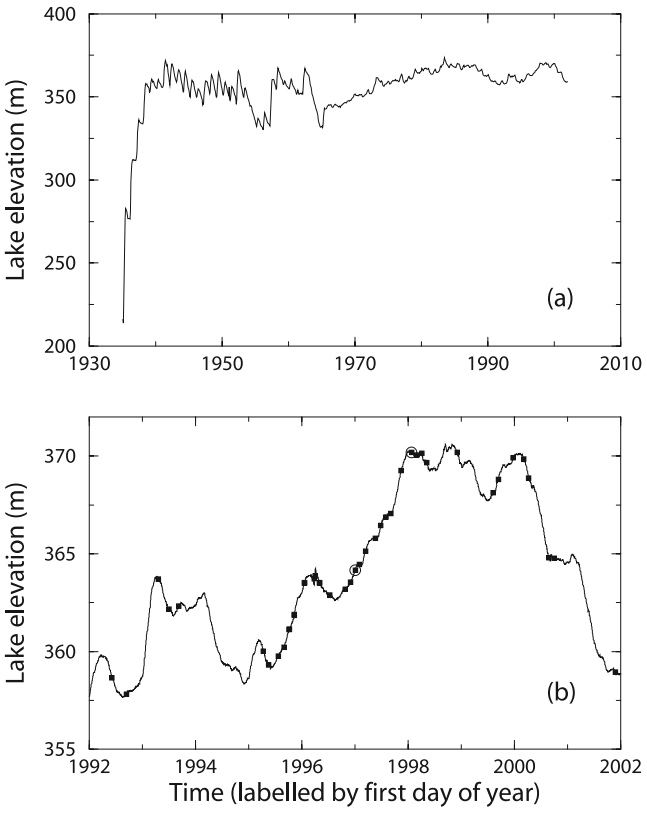

Figure 2. (a) Lake water level evolution between 1935 and 2002 (one data print per month). (b) Enlargement of lake level evolution (one data print per day) during the period covered by ERS radar images. Data come from the Bureau of Reclamation of Boulder city (Nevada). Black squares show the water level at the acquisition dates of ERS scenes. The two dates associated with open circles correspond to the images used to form the interferogram of Figure 5.

stay coherent through time. In areas with low global coherence, displacement measurement can be made only where permanent scatterers (PS) exist, which correspond to strongly reflecting targets with an amplitude and phase stable both over a long period of time and for varying viewing angles [*Ferretti et al.*, 2001]. The PS method has proven to be very efficient to measure slow, small-scale ground deformation in urban environments [*Ferretti et al.*, 2000]. In the Lake Mead area, because of arid conditions and of the absence of vegetation, coherence is preserved over the whole area through large periods of time. The PS technique is thus not required. Here, we combine a series of small baseline interferograms to retrieve the temporal evolution of the phase change, for each pixel in a SAR scene [*Berardino et al.*, 2002; *Schmidt and Bürgmann*, 2003].

[7] SAR interferometry accuracy is strongly limited by atmospheric artefacts, partly due to the nonhomogeneous temporal and spatial distribution of water vapor in the troposphere along the electromagnetic wave paths [*Zebker et al.*, 1997; *Hanssen*, 2001]. The atmospheric phase delays affecting interferograms may reach up to two fringes ($\sim$5.66 cm of range change) at places. Therefore they must be estimated and removed from the InSAR signal before retrieving the deformation with a subcentimetric accuracy. An important part of this work is devoted to this task. Atmospheric corrections might be done by exploiting independent data on the amount of water vapor in the troposphere. *Li et al.* [2003, 2005] use GPS, Moderate Resolution Imaging Spectroradiometer (MODIS), and Medium-Resolution Imaging Radiometer (MERIS) data to map the precipitable water vapor (PWV) content in California at a kilometric resolution during the acquisition of radar images. *Webley et al.* [2004] use data from GPS receivers deployed in the Mount Etna area to validate and calibrate a local meteorological model (NH3D) and derive the PWV field. PWV values, obtained by these methods, are converted into wet delays along the radar line of sight (LOS) to correct interferograms. Without any independent data, various strategies have been proposed to mitigate atmospheric artefacts in deformation measurement. Tropospheric delays due to temporal variations of water vapor horizontal stratification [*Hanssen*, 2001] can be estimated using the correlation between phase and elevation [e.g., *Chaabane et al.*, 2004]. Analyzing numerous SAR images help to decipher between a relatively stable deformation, with time and space, and a randomly changing atmospheric pattern. Temporal averaging by stacking N-independent interferograms [*Peltzer et al.*, 2001; *Wright et al.*, 2001] allows to reduce the temporally uncorrelated noise by a $\sqrt{N}$ factor [*Zebker et al.*, 1997]. However, this technique is inappropriate to detect a nonlinear temporal trend in the deformation. Temporal analysis of multiple interferograms, using appropriate smoothing constraints, allows to eliminate the atmospheric component of the signal and retrieve small spatial scale (5×5 km^2) ground motion [*Schmidt and Bürgmann*, 2003]. The accurate measurement of a subcentimetric deformation on a larger spatial scale (50×50 km^2), as expected in the Lake Mead area, remains a difficult challenge. Phase gradients due to ground motion are then much lower than those related to atmospheric delays.

[8] In the following, after a short description of the Lake Mead area, we present our methodology to correct tropospheric phase delays due to temporal variations of water vapor stratification. We then show how residual atmospheric delays are eliminated by a temporal analysis, to retrieve the ground motion associated with the water and sediment load of the lake. The deformation is then discussed in terms of possible elastic or viscoelastic behavior of the upper lithosphere in the study area. See the notation section for parameter definitions.

2. Regional and Geological Setting

[9] Lake Mead is a large interstate reservoir located in the Mojave Desert at the limit between southeastern Nevada and northwestern Arizona (Figure 1). It was impounded in 1935 after the construction of the Hoover Dam. The lake is made of several basins feeded by the Colorado river and its tributaries. The Boulder and Virgin Basins prevail and represent about 60% of the total water volume. The lake has an elevation of $\sim$350 m and is bordered by north-south trending mountain ridges. The elevation of the area, $\sim$700 m on average, increases eastward up to 1500 m on the Colorado Plateau.

[10] The water level in the lake increased by about 140 meters between 1935 and 1938, then displayed interannual fluctuations of at most 30 m (Figure 2a). Since 1935, 15 to 30 m of sediments filled mainly the former, narrow, Colorado River valley. Much thinner, postimpoundment sediments cover the floor of many narrow tributaries of the former Colorado River. North of the lake, the thickness of the sediments that fill the former Virgin River channel is only 1 to 4 m [*Twichell et al.*, 2003].

[11] The lake is surrounded by Precambrian through Tertiary volcanic and intrusive rocks, Tertiary sedimentary strata and Quaternary alluvial deposits [*Twichell et al.*, 1999]. It is located in the central Basin and Range province, a region of active continental extension and strike-slip faulting. It is bounded to the east by the relatively undeformed Colorado Plateau. The extension in the Basin and Range is accommodated by widely spaced, mostly steep dipping, normal faults. The deformation peaked between 15 and 10 Ma and slowed down since 10 Ma [*Wernicke et al.*, 1988, 2004]. A structural analysis of the Lake Mead area fault system suggests that the end of the extension peak occurred at 9 Ma and was followed by right-lateral and then left-lateral strike-slip faulting [*Duebendorfer and Wallin*, 1991]. During the Miocene, the crust was extended by a factor of 2 in the amagmatic zone north of the lake, and by a factor of 3–4 in the southern part of the lake [*Wernicke and Axen*, 1988]. In the latter area, magmatic activity after 9 Ma displays a clear asthenospheric mantle signature [*Feuerbach et al.*, 1993], suggesting a strongly thinned mantle lithosphere. *Zandt et al.* [1995] argue, on the basis of seismic velocity and gravity data, that the lithosphere thickness beneath the Basin and Range at latitude 37°N is on average 60 km, increasing eastward with an abrupt transition under the Colorado Plateau, to reach about 100 km.

3. InSAR Data and Methodology

3.1. Data

[12] The 10-year archive of the ERS-1 and ERS-2 satellites data, provided by European Space Agency (ESA) and

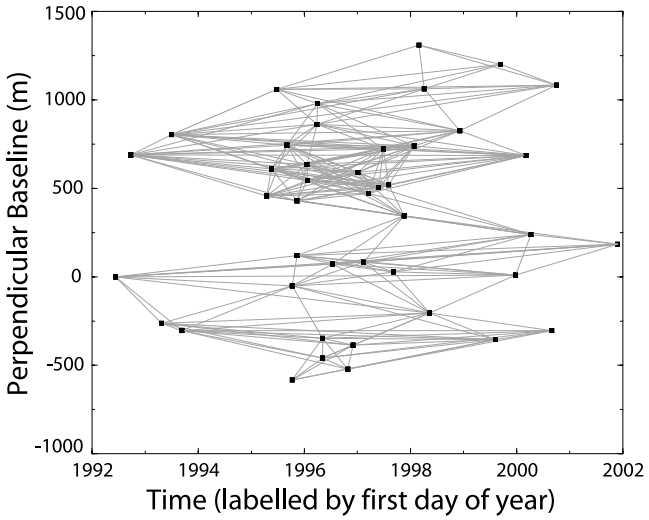

Figure 3. Diagram of available ERS-1/2 images for descending track 84, frame 2877. Relative perpendicular baselines are plotted as a function of acquisition dates. The 43 SAR images are combined into 241 interferograms (grey segments).

centered on Lake Mead consists in 46 ERS images acquired between June 1992 and November 2001 (along descending track 84, frame 2877, Figure 1). Figure 2b shows the temporal distribution of 43 ERS images superimposed on the Lake Mead water level evolution (three images have been discarded in this study due to strong atmospheric phase screen). It illustrates the potential resolution power of our study to measure the deformation associated with lake level fluctuations. In particular, some lake level variations are not sampled by ERS acquisitions. There is a gap of acquisition between September 1993 and April 1995, while two thirds of the acquisitions occur between April 1995 and April 1998 (i.e., during one third of the study period).

[13] We combine the 43 ERS images into 241 interferograms (Figure 3). We select all interferograms with a perpendicular baseline smaller than 200 m, and most interferograms with a baseline ranging between 200 m and 300 m. We use the Jet Propulsion Laboratory/California Institute of Technology ROI-PAC software to process the interferograms [*Rosen et al.*, 2004] and the orbits provided by DEOS [*Scharroo and Visser*, 1998]. The topographic signature is removed using the 1-arc sec Shuttle Radar Topography Mapping (SRTM) digital elevation model (DEM) [*Farr and Kobrick*, 2000]. Interferograms are resampled using 4 looks in range and 20 looks in azimuth (ground pixel are $\sim 80 \times 80$ m^2). To increase the signal-to-noise ratio, a nonlinear spectral filter [*Goldstein and Werner*, 1998] is applied to each interferogram. Because of the high coherence, the phase can be spatially unwrapped on about 80% of the radar scene on average.

[14] The interferometric phase difference between two radar images (slave image minus master image) not only contains the effect of ground motion in the radar line of sight (LOS) but also residual orbital errors, atmospheric delays (Atmospheric Phase Screen, APS), and noise [*Bürgmann et al.*, 2000; *Rosen et al.*, 2000]. A few typical examples of Lake Mead interferograms are displayed on Figure 4, before and after corrections of residual orbital fringes. The amplitude of the phase trend due to errors in orbit estimation is large compared to the expected ground deformation. Once this trend is removed, most interferograms show strong atmospheric artefacts, again of amplitude larger than the expected ground motion, of two types: (1) phase delays correlated with elevation resulting from the temporal variation of water vapor stratification in the troposphere (Figure 4b) and (2) phase delay patterns variable in time and space, in the form of small ripples, blobs, large patches or fronts (Figures 4a and 4d). These atmospheric artefacts

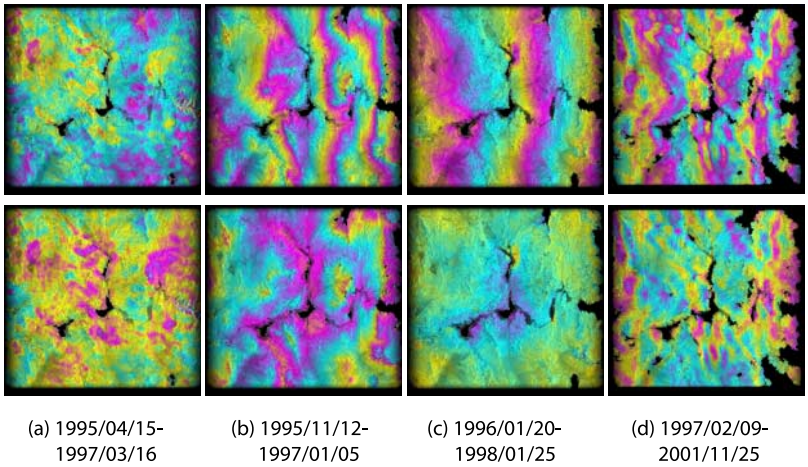

Figure 4. Examples of interferograms displayed in radar geometry (top) before and (bottom) after correction from residual orbit errors. (a) and (d) Interferograms showing numerous atmospheric ripples. (b) Interferogram with a strong phase/elevation correlation. (c) Interferogram devoid of atmospheric artefacts and representing a ground motion signal. The color field displays the phase delay superimposed on the black and white amplitude field. One color cycle (yellow/pink/blue) represents 28 mm of range change along line of sight (LOS) toward the satellite. See scene location on Figure 1.

mask the deformation signal, which is only observed in one particular interferogram (Figure 4c). In the following sections, we describe our methodology to correct individual interferograms from residual orbital fringes and from the effect of the variations in water vapor stratification. Other atmospheric patterns are removed by inverting the global set of interferograms, under the assumption of they being random in time.

3.2. Correction of Residual Orbital Fringes

[15] The accuracy of orbital parameters does not allow to entirely remove orbital fringes during standard interferogram processing. The ROI_PAC software includes an iterative procedure of baseline reestimation, with adjustments either constant, linear, or quadratic as a function of azimuth. However, we choose not to use it in this study. A constant baseline shift clearly does not, in our case, remove all residual orbital fringes. Moreover, the expected deformation contains a large wavelength signal that could be interpreted in the ROI_PAC procedure as residual orbital errors using a baseline adjustment linear or quadratic with azimuth. The elevation also has a large wavelength trend within the ERS scene as the lake, centered on the radar scene, corresponds to a topographic depression (Figure 1). Consequently, atmospheric phase delays correlated with elevation may also be mistaken for orbital errors by the baseline reestimation procedure.

[16] To remove the residual orbital errors, φ_0, we first estimate the best fitting "twisted plane" to the image four borders, away from the deformation zone. Borders are defined by 5×5 km^2 adjacent boxes along image contour. The "twisted plane" is in the form of $\varphi_0 = (ax + b)y + cx + d$, where x and y are the weighted center coordinates in range and azimuth of these boxes. a, b, c, and d are obtained by a least squares minimization of the phase difference $(\overline{\varphi} - \varphi_0)$, where $\overline{\varphi}$ is the median of the weighted phase data within each box. We set the weight of each individual phase data as depending on the local spatial coherence. The "twisted plane" is finally removed from the whole interferogram. With this procedure, flattened interferograms provide a deformation estimate relative to the image borders, where the phase is nearly zero.

3.3. Correction of Phase Delay due to Water Vapor Stratification

[17] The correlation between range change and elevation is due to the variation between two SAR acquisitions of the average water vapor content in the lowermost atmosphere [*Hanssen*, 2001]. The water vapor in the troposphere induces a "wet" delay in the radar microwave back and forth propagation. For a vertically stratified water vapor content over a flat terrain, this delay is homogeneous in space. However, if elevation changes across the scene, the "wet" delay varies with elevation with a rate (delay over elevation) increasing with the water vapor amount. Therefore a change in the troposphere water vapor content between two SAR acquisitions induces a differential "wet" delay varying with elevation, named here the "tropostatic" delay.

[18] Figure 5a shows an example of interferogram affected by such a delay. The global positive correlation between phase delay and elevation (Figures 5b and 5c) implies that the absolute humidity in the bottom atmospheric layer was smaller at the acquisition time of the slave image than at the acquisition time of the master image. In this case, as in many other interferograms, phase elevation correlation masks entirely the ground motion associated with lake level fluctuations (Figure 5d) and needs to be corrected.

[19] A detailed analysis of the relationship between phase and elevation shows that it is mostly linear within the elevation range of the region. Nonlinear trends are not clear enough to be robustly estimated. For 50% and 25% of the interferograms, the linear phase/elevation correlation coefficients are larger than 0.5 and 0.7, respectively. Lower values appear when the tropospheric water vapor stratification is similar for both acquisitions, or when the "noise" (such as local tropospheric turbulence patterns, large-scale atmospheric patches) or the deformation signal is strong.

[20] In many cases, the phase/elevation relationship is better defined locally (over small areas) than globally (on the whole scene). The local relationships may also vary across interferograms. However, we cannot reasonably constrain spatially heterogeneous phase/elevation relationships everywhere on the image, due to possible local trade-off with the deformation/elevation relationship. The most robust procedure that can be applied to all interferograms is thus to estimate the tropostatic delay by a simple global linear regression between phase and elevation. All data points are used, excluding those located close to the lake, where the expected deformation is maximum and partly correlated with elevation. Note that it means we did not correct for a possible evaporation process in the lake area.

3.4. Iterative Corrections of Orbital and Tropostatic Errors

[21] Because elevation is not uniform along the scene contour, the estimate of residual orbital errors is biased by the phase/elevation correlation. We thus iteratively apply both orbital and tropostatic corrections. The first step is to remove the residual orbital fringes, then calculate the phase/elevation correlation. The second step is to subtract the linear phase/elevation trend from the original interferogram, improve the orbital correction, then add again the phase/elevation relation. In a third step, the regression between phase and elevation is reestimated on the newly flattened interferogram. Steps 2 and 3 are repeated twice. This procedure improves the phase/elevation correlation coefficient by about 0.1 on average.

3.5. Inversion of Tropostatic Corrections

[22] The slope of the linear regression between phase and elevation (noted S_{ij}) can be expressed as the difference between two phase/elevation slopes, characterizing the water vapor content in the troposphere at acquisition dates of the master, S_i, and slave, S_j, images ($S_{ij} = S_j - S_i$). The linear inversion of the slopes obtained for all interferograms (S_{ij}) allows to retrieve the relative slope characterizing each image (S_l). The inversion uses the redundant information contained in the interferograms set (241 interferograms made from 43 images) to better constrain the tropostatic delay of each SAR image. We solve for

$$\mathbf{d} = \mathbf{G}.\mathbf{s} \tag{1}$$

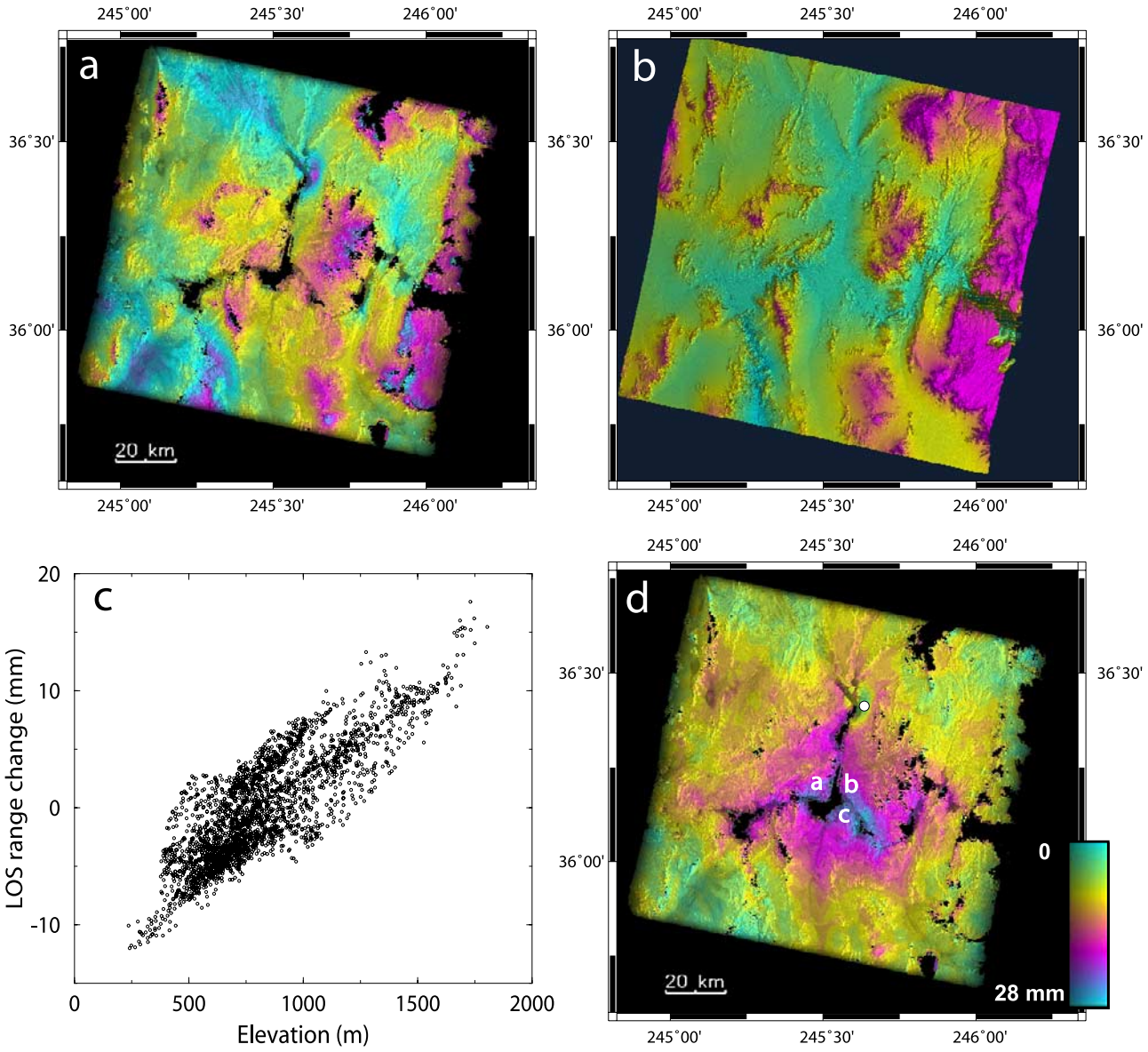

Figure 5. (a) Interferogram 1997/01/05-1998/01/25 showing evidence of phase/elevation correlation. (b) Corresponding topography from SRTM DEM. One color cycle (blue/green/pink) represents the elevation between 250 m and 2000 m. (c) LOS range change as a function of elevation, excluding areas close to the lake. (d) Interferogram after correction from a linear phase change with elevation (see text). It displays the LOS ground subsidence due to the lake level increase (7 m) between the two acquisition dates (Figure 2b). In Figures 5a and 5d, one color cycle (yellow/pink/blue) represents 28 mm of range change along LOS away from the satellite.

where **d** contains the N regression slopes, S_{ij}, for the N interferograms, **s** contains the M unknown slopes, S_l, for the images, and **G** is a $N \times M$ matrix. The elements G_{kl} are equal to 1 if $l = j$ and -1 if $l = i$, 0 otherwise, where j and i are the slave and master images of interferogram k. The above system is underdetermined because the absolute slope for each image cannot be computed. The constraint $\Sigma_l S_l = 0$ is added to equation (1) in the least square inversion. The values of S_l plotted as a function of acquisition date (Figure 6) show a slight trend toward more humid conditions with time, which is due to a nonhomogeneous sampling of humid and dry days along years. "Humid" images occur both during winter and during monsoon in summer. Finally, each interferogram is corrected for the tropostatic effect using the difference, $S_j - S_i$, between the inverted slopes of the slave and master images.

[23] Similarly, we compute the error, σ_{Sl}, on the inverted slopes, S_l, from the error estimated on the interferogram slopes, σ_{Sij}. σ_{Sij} is computed from the variance/covariance of the phase and elevation data sets. We approximate σ_{Sij} as the sum of the errors of the master (σ_{Si}) and slave (σ_{Sj})

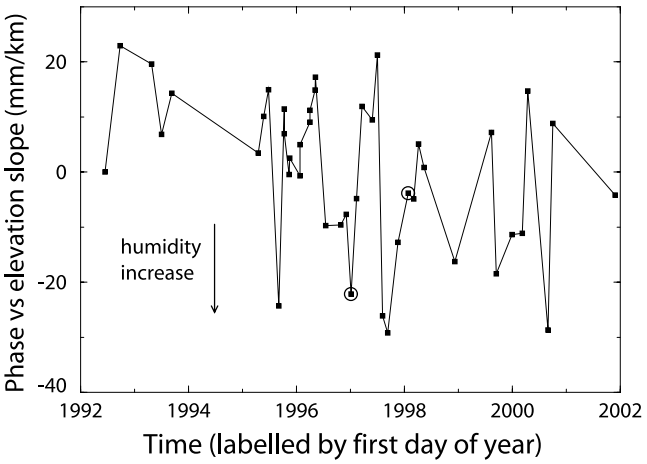

Figure 6. Phase versus elevation slopes, S_l, obtained at each acquisition date, relative to the first image. Humidity increases toward lowest values. The two open circles correspond to the interferogram dates of Figure 5.

images, and we obtain by inversion an estimate of the absolute error σ_{Sl} on S_l (see error bars on Figure 7a).

3.6. Validation of Tropostatic Corrections

[24] The relative classification of the atmospheric water vapor content at all acquisition dates, given by S_l (Figure 6), can be validated using independent meteorological data, taken from the global reanalysis atmospheric model ERA40. This model, built by the European Centre for Medium-Range Weather Forecasts (ECMWF), has a one degree, four times daily, resolution [*Uppala et al.*, 2005]. We extracted from ERA40 the total column water vapor (TCWV in kg m^{-2}), the surface temperature (T_{2m}, at 2 m), and the specific humidity by unit air mass, q_a (in kg kg^{-1}) at different pressure levels (0.775 to 1 bar), at 36°N, 114°W, and 1800 UT for each ERS acquisition date. We parameterize the lowermost atmosphere water vapor content by unit air volume, $\overline{q_a}$ (in kg m^{-3}) by the pressure integral of the specific humidity, q_a, over the model pressure, p, levels (between p_b = 1 bar and p_t = 0.775 bar)

$$\overline{q_a} = \frac{1}{H}\int_0^H q_a \rho dz = \frac{1}{gH}\int_{p_t}^{p_b} q_a dp \qquad (2)$$

where z is the elevation, g is the gravity acceleration, ρ is the atmosphere density, and H is the integration height. The good correlation coefficient (0.71) between the phase/elevation slopes, S_l, and the integrated specific humidity, $\overline{q_a}$, validates a posteriori our tropostatic corrections. We find that S_l (mm km^{-1}) = $-4360\ \overline{q_a} + 19.4$.

[25] However, in ERA40, TCWV is better known than specific humidity layering. The height scale, h_W, of the humid atmosphere can be derived from ERA40 using h_W = TCWV/ρq_a where ρq_a is here taken at 1 bar. During the 1992–2002 period, it varies from about 1100 m at low temperature (280 K) to about 2600 m at high temperature (305 K). An analysis of all data at 36°N, 114°W and 1800 UT shows that h_W can be parameterized by $h_W = 1.0185 \times 10^5 - 727.5\ T_{2m} + 1.317\ T_{2m}^2$ (h_W in m, T_{2m} in K). Hence the bottom atmosphere specific humidity at our 43 acquisition dates can be expressed by the ratio TCWV/h_W, h_W being derived from the above relation. We find the relation $S_l = -3924$(TCWV/h_w) + 24.4, with an improved regression coefficient of 0.84 (Figure 7a).

[26] The phase/elevation slopes predicted from the ERA40 model using the calibration relation above (Figure 7a) are comparable to the slopes computed from interferograms (Figure 7b). Both show a nonnegligible pluriannual trend with time. This trend is shown on Figure 7b, fitted with a third-order polynome. It is clearly more pronounced using the InSAR data than using ERA40. The more humid conditions (in average) at acquisition dates

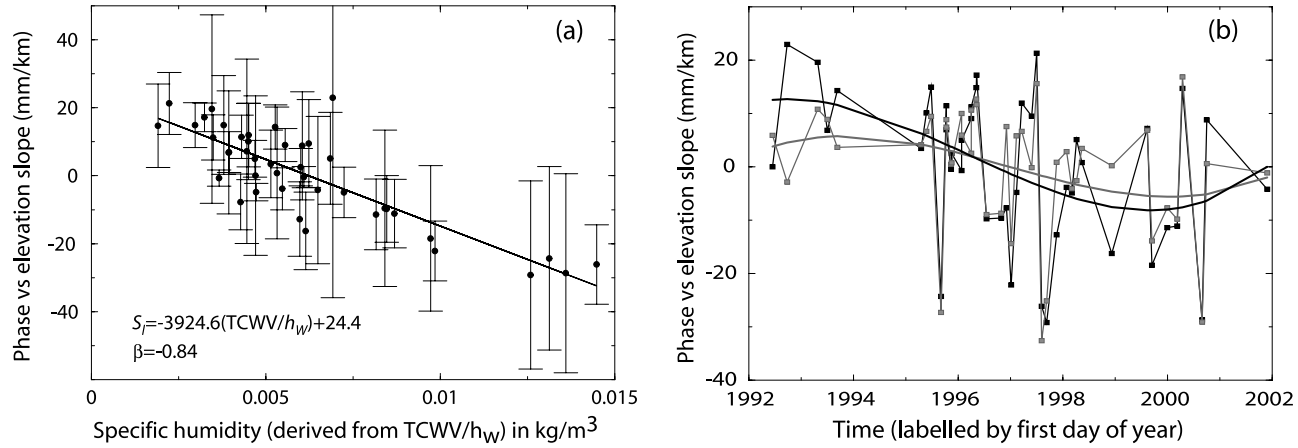

Figure 7. (a) Comparison between elevation versus phase slopes, S_l, obtained for each image and the specific humidity extracted from ERA40 global atmospheric model. Specific humidity at 1 bar is derived from TCWV/h_w, where TCWV is the total column water vapor and h_W is the water vapor height scale. The black line is the regression line, β is the correlation coefficient. (b) Comparison between the elevation versus phase slopes obtained for each image from InSAR data inversion (black line with squares) and derived from the ERA40 global atmospheric model, calibrated by the relation in (Figure 7a) (grey line with squares). Black and grey lines without dots correspond to third-order polynomial fits.

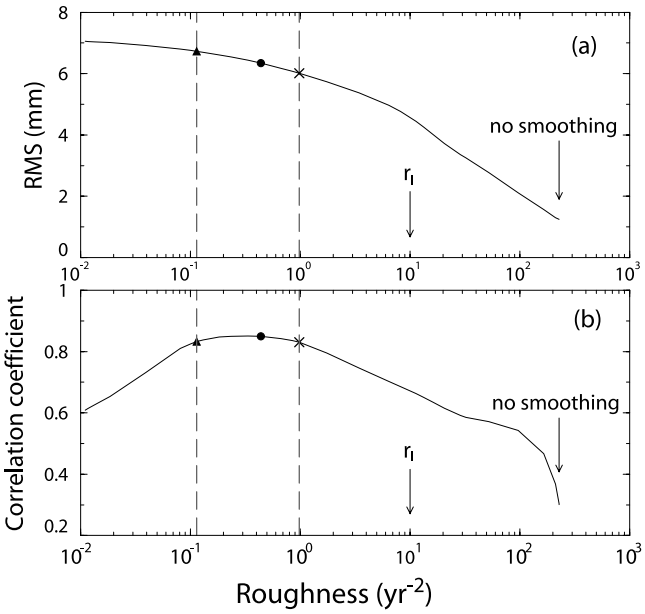

Figure 8. (a) RMS between original and reconstructed interferograms and (b) correlation coefficient between ground motion temporal evolution and lake level variations, plotted as a function of the retrieved ground motion roughness. The correlation coefficient value is taken as the median value of the pixels located in the image central area. Dashed lines bracket roughness interval tested in our inversions. The solid triangle, solid circle, and cross correspond to minimum, preferred, and maximum roughness, respectively, displayed in Figures 9 and 10; r_l indicates the roughness value of the lake level variations sampled at acquisition dates.

in 1998–2000 correspond to a high lake level thus to a subsidence period around the lake. This implies that tropostatic corrections may include part of the deformation signal. This problem will be discussed further in section 4.4 by comparing estimated ground motions using both types of tropostatic corrections.

4. Data Inversion

4.1. Inversion Method: No Smoothing

[27] Corrected interferograms are inverted to solve for the incremental deformation between two successive images using a least squares inversion method [*Menke*, 1989]. For each pixel, treated independently from its neighbors, we solve

$$\mathbf{d} = \mathbf{G}.\mathbf{m} \tag{3}$$

where **d** includes N interferograms observations, **m** corresponds to M-1 incremental displacements between the M time steps, and **G** is a N by M-1 matrix containing zeros and ones, based on the stating that the interferometric phase, φ_{ij}, is the sum of successive phase increments between image i and image j: $\varphi_{ij} = \sum_{k=i}^{j-1} m_k$. Images are ordered by dates. This inversion is applied to a very large number of pixels at almost all time steps. However, because some SAR images provided by ESA have missing data bands, and because some interferograms have incoherent areas, inversion cannot be performed for all pixels within all interferograms and between all time steps. The number of interferograms, N, and the number of images, M, are then reduced in the inversion to N_i and M_i, where N_i and M_i depend on the inverted pixel. For the few pixels for which the system (3) is underdetermined, a single value decomposition technique is used in places of the least squares minimization.

[28] The inversion uses the redundant information of the 241 interferograms to reduce some errors due to interferogram formation. We evaluate the system misclosure for each pixel by the RMS:

$$\varphi_{RMS} = \frac{1}{N}\left[\sum_{N}\left(\varphi_{ij} - \sum_{k=i}^{j-1} m_k\right)^2\right]^{1/2} \tag{4}$$

where φ_{ij} is the measured interferometric phase between image i and image j, and $\sum_{k=i}^{j-1} m_k$ is the reconstructed phase between the same dates. The misclosure is about 1.25 mm in average (Figure 8a) and is mainly due to geometric decorrelation, filtering effects in areas of low coherence, and possible local unwrapping errors. We eliminate incoherent pixels for which the misclosure exceeds a fixed threshold of 3.5 mm. The RMS sum over all P pixels of a given interferogram, defined by $\frac{1}{P}[\Sigma_P(\varphi_{ij} - \sum_{k=i}^{j-1} m_k)^2]^{1/2}$, allows to detect and eliminate three interferograms presenting unwrapping errors. Finally, we can reconstruct interferograms using $\sum_{k=i}^{j-1} m_k$, between any two images i and j, independently of the baseline. The stack of reconstructed interferograms, all computed with a common master image, emphasizes the APS of each individual image. The amplitude delays (in mm) of atmospheric perturbations across the stacks give the images APS amplitude, $|\mathrm{APS}_I|$.

4.2. Inversion With Smoothing

[29] The time series filtering used in this study to decrease the influence of random APS differs from that of *Ferretti et al.* [2001] or *Berardino et al.* [2002], as we cannot make a priori assumptions on the deformation behavior with time. We prefer to introduce temporal smoothing in the inversion as another constraint, by minimizing the curvature of the inverted phase temporal evolution [*Schmidt and Bürgmann*, 2003]. Additionally, a term proportional to the baseline is included in the inversion to limit the effect of DEM errors. Note that although these errors might be negligible for baselines lower than 300 m, they may cumulate in the inversion as the cumulative baseline reaches ~2000 m. The system becomes

$$\begin{pmatrix} \mathbf{d}' \\ 0 \end{pmatrix} = \begin{pmatrix} \mathbf{G}' & \mathbf{b}' \\ \gamma^2\omega_i \frac{d}{dt^2} & 0 \end{pmatrix} \cdot \begin{pmatrix} \mathbf{m} \\ e_{DEM} \end{pmatrix} \tag{5}$$

where **b** is the perpendicular baseline vector and e_{DEM} is the proportionality coefficient between phase and baseline due to DEM errors; **d**, **G**, and **b** are weighted by the matrix **W** (**d**′ = **Wd**, **G**′ = **WG**, and **b**′ = **Wb**); γ is the smoothing coefficient introduced to ponderate the minimum curvature constraints dm/dt^2 (where t is time); $dm/dt^2|_i$ is evaluated

with a five-point finite difference scheme centered on each acquisition date i. On the early side of the time series, we apply the boundary condition $m/dt = 0$ to minimize the displacement between the first two images, which have close water levels and a large APS. On the late side, we compute dm/dt^2 with a backward finite difference scheme. The weight, **W**, applied on each interferogram is the product of two terms: (1) the first term equalizes the weight of all images in the inversion and (2) the second term characterizes the interferograms "quality", q_{ij}, defined as the inverse sum of both images i and j APS amplitudes: $q_{ij} = 1/(|\mathrm{APS}_i| + |\mathrm{APS}_j|)$.

[30] The strategy for smoothing this highly irregularly sampled data set (time increments between 1 day and 1.6 years) results from the trade-off between (1) the desired temporal resolution of retrieved ground motion fluctuations and (2) the APS removal. If we want option 1 to be homogeneous across the time series, $dm/dt^2|_i$ must be weighted by $\omega_i = 1$. On the contrary, if we want option 2 to be homogeneous through the time series, $dm/dt^2|_i$ must be weighted by $\omega_i = \overline{\Delta t_i}^2$ (where $\overline{\Delta t_i}$ is the mean time interval across the five-point differential operator). After testing, we choose an intermediate solution, given by $\omega_i = \overline{\Delta t_i}$, for which APS removal is not negligible for widely spaced acquisitions and for which ground motion is not allowed to vary too much between densely spaced acquisitions.

4.3. Role and Choice of the Smoothing Level

[31] It is quite arbitrary to decide which smoothing amount (γ in equation (5)) is necessary to decrease the influence of random APS without loosing too much signal (temporal resolution and amplitude). To settle a choice, we first parameterize the roughness (or inverse smoothness) of the temporal evolution of the estimated ground deformation by

$$r_m(\gamma) = \frac{\sum_{i=1}^{M} |\omega_i \frac{dm}{dt^2}|}{\langle \sigma_m \rangle \sum_{i=1}^{M} \omega_i} \quad (6)$$

where $\langle \sigma_m \rangle$ is the standard deviation of cumulative displacement. Low roughnesses correspond to very smooth solutions, which asymptotically reach a linear displacement in time. The roughness is equal to the original data roughness for $\gamma = 0$ ($r_m(0) = 228.42$ yr^{-2}), and decreases as γ increases. For comparison, the roughness of the lake level variations, r_l, is estimated with the same formula (equation (6)), replacing m by the increments in lake level between successive acquisition dates. Note that lake level fluctuations are clearly smoother, with $r_l = 10$ yr^{-2}, than original interferometric data, which are controlled by random APS (Figure 8).

[32] To help choosing the smoothing level, we plot on Figure 8, as a function of roughness, $r_m(\gamma)$, the evolution of the RMS between "true" and "reconstructed" interferograms (φ_{RMS}, equation (4)), and of the correlation coefficient, β, between inverted cumulative displacement and lake level fluctuations. As roughness decreases, φ_{RMS} increases monotically from its value without smoothing (1.25 mm) to ~7 mm, about the variance of the interferometric phase (~7.22 mm). The correlation coefficient, β, increases from about 0.3 without smoothing to a peak value of 0.85 as smoothing increases, and finally drops at very low roughness. The solution obtained with the same roughness as that of the lake level fluctuations, r_l, still corresponds to a low correlation coefficient ($\beta = 0.67$), indicating that APS removal is not efficient enough. Therefore we choose to loose some temporal resolution and select solutions smoother than the lake level fluctuations, which have correlation coefficients larger than 0.83 (roughness interval between 0.11 yr^{-2} and 0.98 yr^{-2}, Figure 8). Our preferred solution (black dot on Figure 8) corresponds to a high φ_{RMS} value, which means that residual phase delays of atmospheric origin are much larger than the retrieved ground motion.

[33] Figures 9a, 9b, and 9c show three ground motion time series for three roughness values of 0.11 yr^{-2}, 0.44 yr^{-2}, and 0.98 yr^{-2}, respectively. The high roughness solution exhibits short term jumps that may suggest that APS smoothing is not efficient enough. This is confirmed by variable spatial heterogeneities still present in the inverted LOS motion maps. The low roughness solution is too smooth, resulting both in a lack of temporal resolution and in a lowered amplitude. However, spatial APS patterns are efficiently removed, except for the last acquisition date. Finally, our preferred choice, with the best compromise between temporal resolution, retrieved deformation amplitude, and APS removal, has a roughness of 0.44 yr^{-2} and a correlation coefficient between ground motion and lake level fluctuations of 0.85.

[34] To illustrate the smoothing effect on the time series, we smooth the lake level variations to reach the same roughness values of 0.11, 0.44, and 0.98 yr^{-2}. Smoothing is performed as described by equation (5), without the baseline terms $\mathbf{b}'$ and e_{DEM}. We replace the interferometric phase in **d** by water level changes between the same acquisition dates. Figure 10 shows that the low roughness solution significantly underestimates the true lake level variations in agreement with the trend depicted on Figures 9a, 9b, and 9c. Our preferred roughness value returns a slightly lowered signal amplitude with a reasonable loss in temporal resolution.

4.4. Error Estimation

[35] Error on the ground motion estimation is difficult to constrain. The error on the phase itself is relatively low and can be estimated to about a millimeter by computing the interferometric system misclosure. However, the APS constitutes by far the main source of error, and is strongly irregular in shape, amplitude, and wavelength (Figure 4). Furthermore, as stated before, the deformation signal is low with respect to atmospheric delays. As the APS is here removed (step a) by the tropostatic correction and (step b) by temporal smoothing, estimating errors on the time series implies to quantify how well we can perform these two steps with a minimum signal loss. The comparison of the time series performed with various levels of smoothing (Figures 9a, 9b, 9c, and 10) likely yields the best semi-quantitative insight about the possible error related to step a.

[36] The sensitivity of retrieved deformation to step b is tested using tropostatic corrections derived (case b1) from independent and calibrated ERA40 humidity data (see section 3.6) and (case b2) from InSAR. Deformation time series are compared in Figure 11 for a point located close to

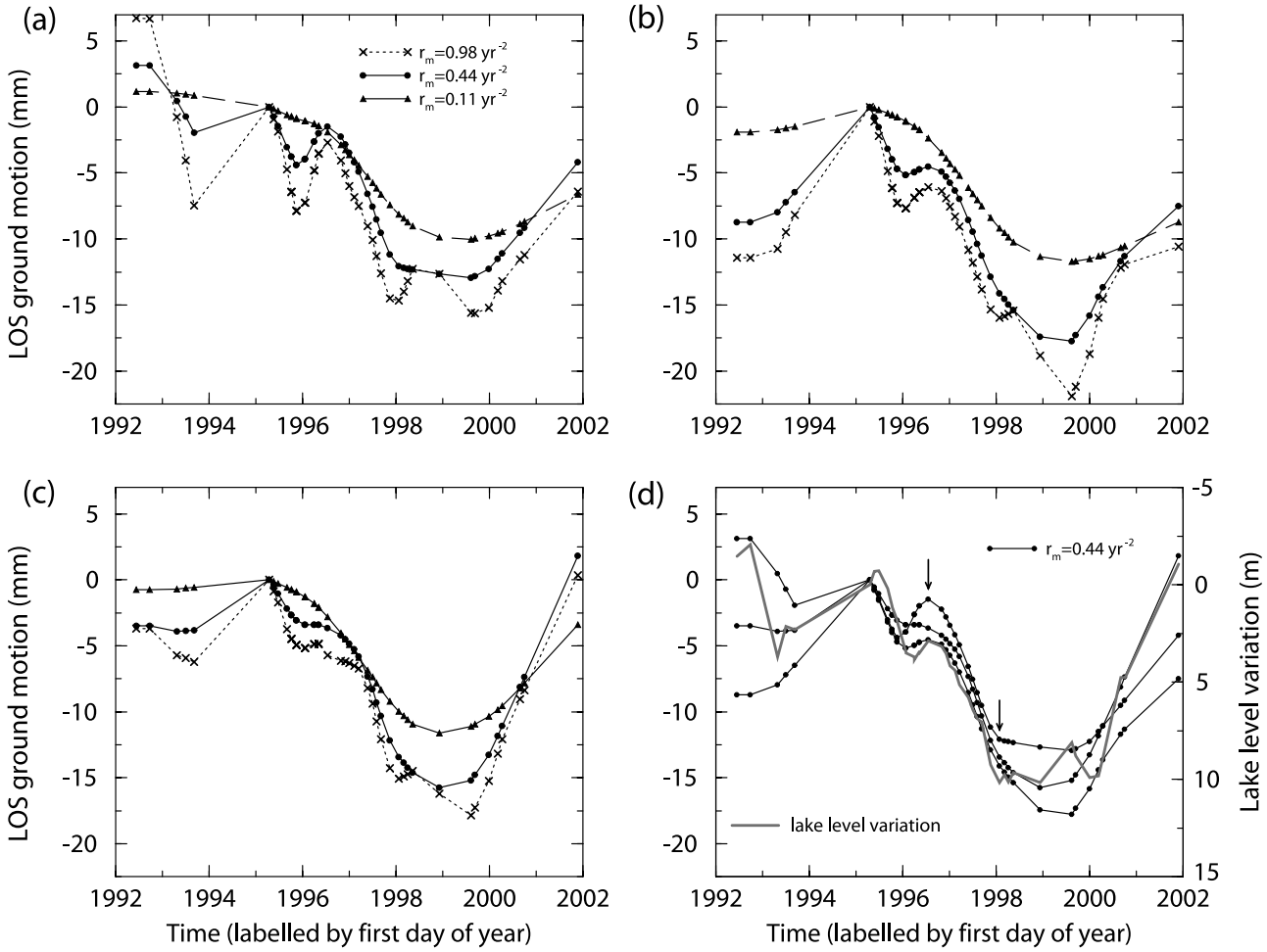

Figure 9. (a), (b), (c) Retrieved ground motion through time for three roughness values, r_m, and three locations close to the lake center (see white labels on Figure 5d). (d) Comparison of lake level fluctuations with ground motion variations for the three locations close to the lake center. Arrows define the time interval for ground motion depicted in Figure 12. Note that the y axis for lake level variations has been flipped.

the lake center. The amplitude of the ground motion is significantly larger in case b1. This is consistent with the pluriannual trend difference observed between cases b1 and b2 sets of phase/elevation slopes (Figure 7b). This might suggest that the tropostatic corrections derived from InSAR data are overestimated and partly include some deformation signal. However, deformation maps in case b2 do not show any correlation with elevation, in contrast to the slight correlation with elevation displayed by deformation maps in case b1). Our preferred solution thus remains that based on the tropostatic correction inferred from InSAR data. It might anyhow be considered as a lower bound for ground motion amplitude.

5. Inversion Results Analysis

[37] Figure 9d shows the temporal evolution of the LOS motion in three selected areas close to the Lake Mead center. These areas subside as water level increases, and uplift when water level decreases (Figure 9d). The correlation coefficient between retrieved ground motion, obtained after temporal smoothing (roughness equal to 0.44 yr^{-2}), and lake level fluctuations is 0.85. A subsidence of about 16 mm is observed during the 1995–1998 period corresponding to a lake level increase of 11 m. It is followed by an uplift of similar amplitude from the beginning of year 2000, as the water level dropped back to its 1995 level. Note that the 1995–1998 period is well covered by ERS images, allowing a better sampling of the deformation signal, hence measured with a greater accuracy. Figure 12 displays the deformation map between July 1996 and January 1998 (dates shown by arrows on Figure 9d). It is clearly dominated by a large wavelength pattern that can be interpreted as ground subsidence in response to the lake loading. The profile across the scene shows that the subsidence sharpens when crossing the lake arm. The good match between the retrieved ground motion and lake level fluctuations suggests that the deformation shown in Figure 12 is an elastic response to the lake loading. However, as we will see section 5, this is not supported by the modeling.

[38] The deformation map (Figure 12) reveals that ground motions are not homogeneous around the lake. Note in particular an oval shaped area of uplift ($\sim 20 \times 10$ km^2) north of the lake. Contrary to the large-scale ground motion,

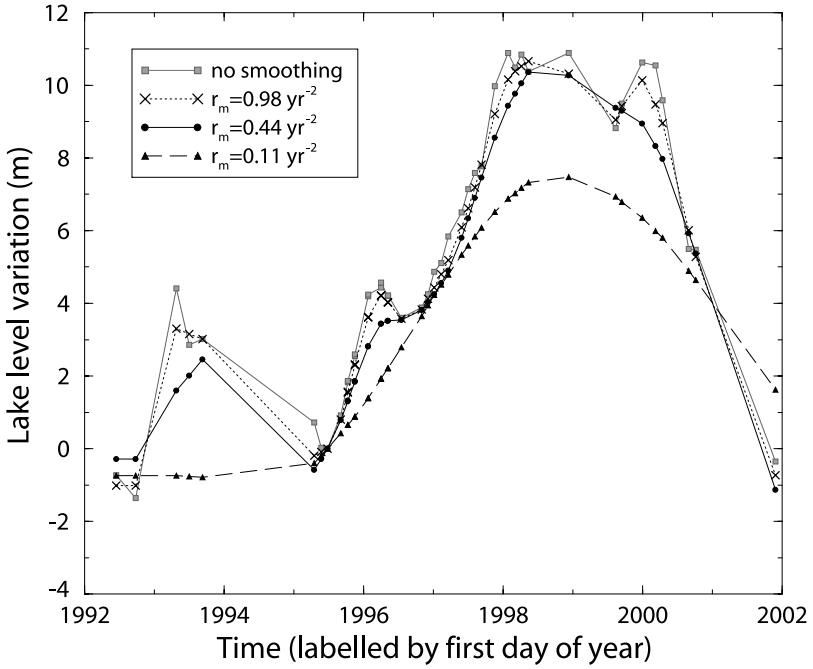

Figure 10. Effect of smoothing on lake level variation sampled at image acquisition dates (grey line with squares), obtained for the same roughness values, r_m, as shown by symbols on Figure 8.

this local ground displacement is clearly seen on numerous individual interferograms (see examples on Figures 4 and 5). The time series reveals that this local motion is correlated with the lake water level (Figure 13): The maximum uplift is recorded between 1995 and 1999 with 15.5 mm of LOS range change, as the lake level increased. We note a small temporal delay between water level change and ground motion. This deformation most likely arises from the poroelastic response of a sedimentary layer adjacent to the lake, in which the groundwater communicates with the lake. A high lake level may induce, after some delay due to pore pressure diffusion, an increase of the water table in the adjacent sedimentary layer, therefore a poroelastic uplift of the sedimentary layer surface. Other smaller areas near the lake show similar, local ground movement which does not follow the main deformation trend. Independently, we also observe a continuous uplift (of up to 2 cm) near Las Vegas, during the period 1992–2002. This ground motion results from the aquifer system deformation [*Amelung et al.*, 1999].

[39] This study thus shows the feasibility of measuring a subcentimetric ground motion with a nonlinear behavior in time over a large area, associated with lake level fluctuations. On the same frame, we detect two types of deformation of comparable amplitude but different spatial scales:

[40] 1. The deformation at a smaller scale is directly observed on numerous interferograms, even if orbital ramp or atmospheric artefacts remain on the interferograms. Indeed, larger deformation gradients associated with smaller-scale ground motions are detected even when superimposed on random atmospheric patterns with moderate phase gradients. Moreover, elevation changes across a small area are likely to be small, making tropostatic corrections of little importance.

[41] 2. On the contrary, the deformation at a larger scale is masked on all but one interferogram by APS. In conclusion, the ground motion over small areas can be detected with or without smoothing constraints, whereas over large areas corrections of residual orbital errors and tropostatic effects, as well as data smoothing, are crucial to retrieve the large-scale ground motion associated with lake loading.

6. Model

[42] The high correlation coefficient between lake level variations and the retrieved ground motion (0.85) would

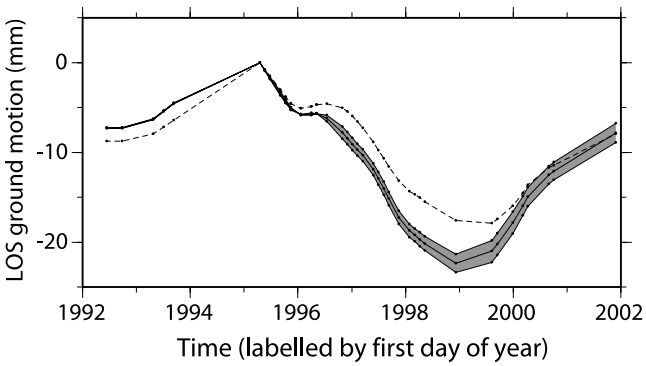

Figure 11. Comparison of the deformation temporal evolution retrieved when tropostatic corrections are derived from InSAR data (dashed line, see Figure 9b) or from ERA40 model (grey area). The roughness is in all cases equal to 0.44 yr^{-2}. Tropostatic corrections derived from ERA40 model have been qualibrated using the relation shown in Figure 7a (central curve in grey area). The deformation retrieved after setting a larger or a lower qualibration factor (plus or minus 30%) is shown by the two curves delimiting the grey area.

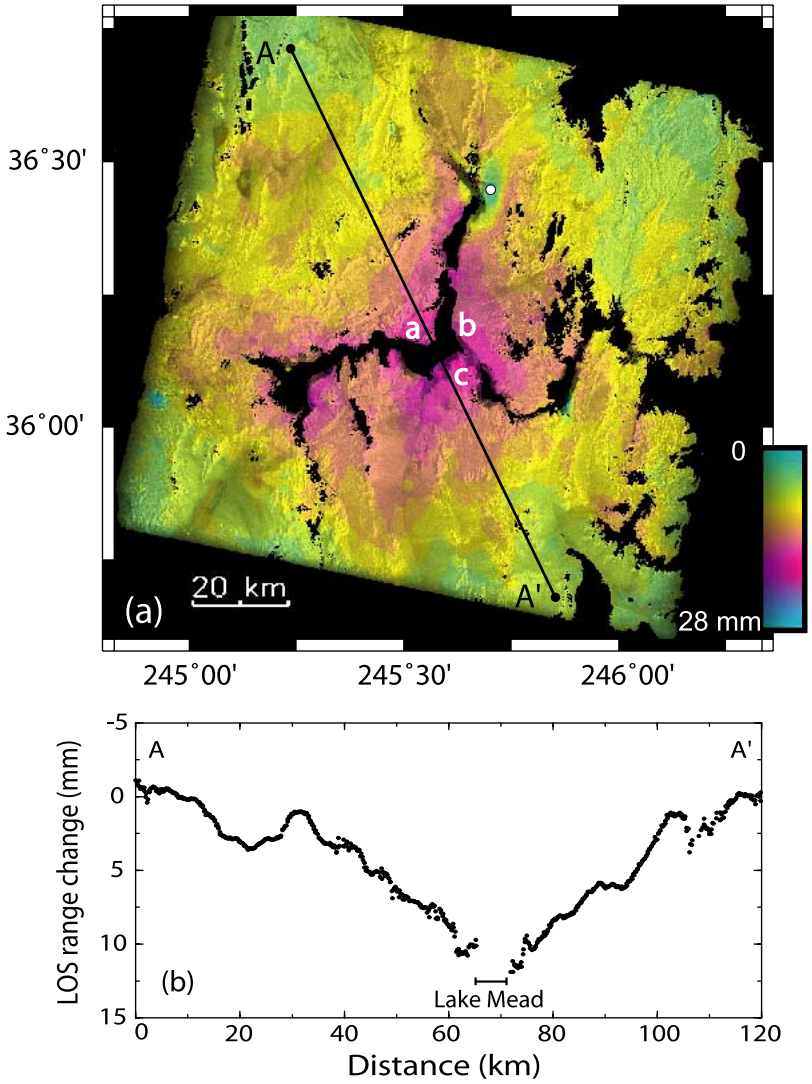

Figure 12. (a) Reconstructed interferogram between July 1996 and January 1998 (see arrows on Figure 9d). One color cycle represents 28 mm of range change along LOS as defined in Figure 5. (b) Profile (black line on Figure 12a) across the scene.

suggest that the lithosphere responds instantaneously to the load on a decade time scale due to its elasticity. To test this hypothesis and discriminate between an elastic or a viscoelastic deformation (using the parameters published by *Kaufmann and Amelung* [2000] for the Lake Mead lithosphere), we build a model taking into account the well known lake loading history since 1935. We show first that beyond doubt, the retrieved ground motion can be attributed to the lake loading. Second, we test how a few forward models fit the retrieved ground motion. However, it is beyond the scope of this paper to invert for the viscoelastic parameters of the lithosphere. The model equations and resolution method are given in Appendix A.

6.1. Setup

[43] We consider a Maxwell viscoelastic prestressed body organized in two or three layers in a 3-D Cartesian box. Each layer, i, is defined by its thickness, h_i, the Lamé parameters, μ_i and λ_i, and the viscosity, η_i (Table 1). The code is based on the correspondence principle between elastic and viscoelastic bodies and on the spatial and temporal Fourier decomposition (see Appendix A). At wavelengths concerned in this study, the self-gravitation term is negligible.

[44] The load history take into account the lake level changes since the impoundment and the progressive sedimentation in the lake. Note, however, that the sediment load contribution is very small with respect to the water loading. A detailed elevation map of the lake floor is provided by *Twichell et al.* [2003] with a resolution of 10 m × 10 m in UTM projection. We build the spatiotemporal load model by filling the lake floor DEM to a given lake level. The load model is decimated to a spatial resolution of 2 km × 2 km by integrating the load from the fine to the rough mesh, and sampled every two months from 1935 to 2002. The Fourier spatiotemporal decomposition of the load assumes it to be periodic in time and space. Therefore the load is extrapolated by zero padding on a 500 km × 500 km wide area and over a 285-year-long period. We verify that these time and space windows are large enough for the assumed load

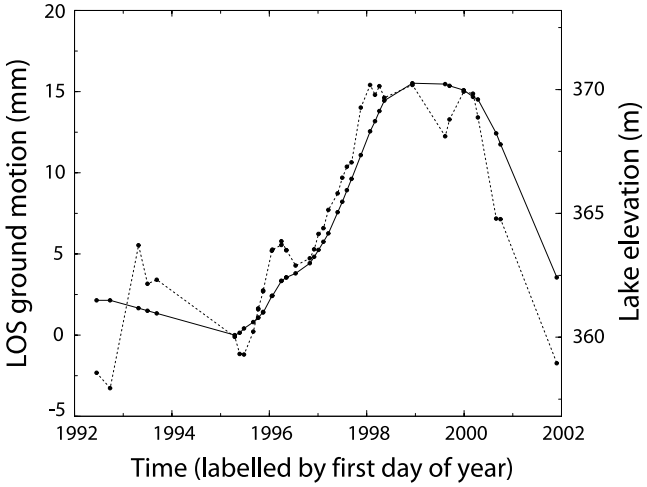

Figure 13. Displacement evolution through time (solid line) obtained from data inversion in the "anomalous" area located north of the lake (see white dot on Figure 5d). The ground motion is measured here with respect to adjacent "normal" area. It is correlated, with a slight delay, with lake level variations (dotted line).

periodicity not to affect the modeled deformation. For a purely elastic upper mantle, the deformation responds instantaneously to the load, and does not depend on the chosen time window. For a viscoelastic upper mantle, the chosen time window must be long enough for the stress to completely relax from one loading cycle to the next. This is true here, except for a viscosity of 10^{19} Pa s, for which a residual continuous subsidence of less than 0.1 mm/yr subsists at the end of a loading cycle. We also verify that the modeled deformation is insensitive to the chosen box height, here taken as 500 km, with a 3 km vertical grid spacing.

[45] The modeled surface deformation, computed every two months, is interpolated at each ERS acquisition date. The North, East, and Up components of the deformation are then projected along LOS. The modeled LOS ground motion is then flattened to put the scene four borders close to zero, as done for the interferograms. The spatiotemporal model can then directly be compared with InSAR deformation time series.

6.2. Forward Models

[46] The elastic moduli are constrained by the seismic velocity structure inferred for the Lake Mead area, applying the relationships $V_p^2 = (\lambda + 2\mu)/\rho$ and $(V_p/V_s)^2 = (\lambda + 2\mu)/\mu$, where V_p and V_s are the P and S waves seismic velocities (Table 1). In order to test a reasonable range of elastic models, we consider a range of possible seismic velocities and crust thicknesses. The maximum elastic deformation is expected for a low velocity, thick crust and the minimum elastic response corresponds to a high-velocity, thin crust. Seismic reflection experiments in the Lake Mead put the Moho discontinuity at 10–11 s (two-way traveltime) [*Brady et al.*, 2000]. Seismic refraction studies yield an average crustal P velocity of 6.1 km s^{-1}, and a P velocity on top of the lithospheric mantle of 7.8 km s^{-1} [*Roller and Healy*, 1963; *Priestley et al.*, 1980]. The ratio V_p/V_s is obtained from a receiver function study performed 100 km north of Lake Mead [*Zandt et al.*, 1995]. The resulting range for elastic moduli is given in Table 1.

[47] The simplest viscoelastic model proposed by *Kaufmann and Amelung* [2000] (KA) to adjust levelling data yields an elastic thickness of 30 km and a viscoelastic upper mantle with a viscosity of 10^{18} Pa s. Our viscoelastic model (model M2, Table 1) differs in some respects from that of KA (elastic parameters, not given in KA, water load, reference to the geoid surface). However, we check that it reproduces the same delayed ground motion following impoundment as described in KA for the period 1935–1960. We also model, in particular, the delay between the lake impoundment and the ground subsidence.

[48] For comparison, similar viscoelastic models but with a lower (10^{17} Pa s) and a larger (10^{19} Pa s) viscosity are also discussed, together with viscoelastic models with elastic thicknesses larger (22 km) or lower (42 km) than the crust thickness (32 km).

6.3. Temporal Comparison Between Models and Data

[49] Figure 14 displays as a function of time the comparison between the ground motions predicted by elastic

Table 1. Model Parameters[a]

Model	Layer	Viscosity η, Pa s	Shear Modulus μ, GPa	Lamé Parameter λ, GPa	Thickness h, km	P Velocity V_p, km s^{-1}	Moho[b] Discontinuity T_{MOHO}, s
				Elastic Models			
M1a	crust	10^{23}	39.1	40.2	30	6.5	9.23
	mantle	10^{23}	64.1	72.6	∞	7.8	
M1b	crust	10^{23}	33.3	34.2	35	6.0	11.67
	mantle	10^{23}	64.1	72.6	∞	7.8	
				Viscoelastic Models			
M2	crust	10^{23}	35.55	36.53	$\in$ [22,42]	6.2	10.65
	mantle	$\in [10^{17},10^{19}]$	64.1	72.6	∞	7.8	
				Equivalent "Poroelastic" Model			
M3	upper crust	10^{23}	35.55	25.58	15	6.2	
	lower crust	10^{23}	35.55	36.53	17	6.2	10.65
	mantle	10^{23}	64.1	72.6	∞	7.8	

[a] $V_p/V_s = 1.74$ and $\rho_c = 2800$ kg m^{-3} for the crust; $V_p/V_s = 1.77$ and $\rho_m = 3300$ kg m^{-3} for the mantle.
[b] T_{MOHO}, two-way traveltime.

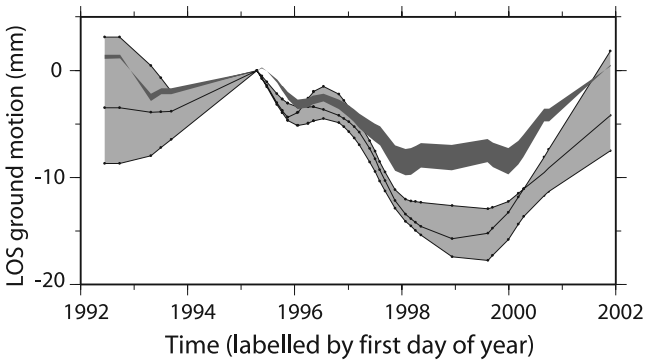

Figure 14. Comparison between the retrieved ground motion (light grey area) and the prediction from elastic models (dark grey area). The three ground motion curves displayed on Figure 9d delimit the light grey envelope. The dark grey area includes the motion predicted for the minimum and maximum interval of possible elastic models and for the three locations close to the lake center shown by white circles on Figure 5d.

models and those retrieved from InSAR. The InSAR deformation is larger than the maximum modeled elastic deformation by a factor of 1.5. This points toward a nonelastic response of the lithosphere in the Lake Mead area on the decade timescale. Figure 15a shows that the simplest viscoelastic model proposed by *Kaufmann and Amelung* [2000] explains both the amplitude and temporal behavior of the retrieved ground motion. The temporal correlation coefficient is better for this viscoelastic model (0.90) than for the elastic model (0.85). Note that in the time window 1992–2001, viscoelastic temporal delays between lake level change and modeled ground motion are very small and thus cannot be detected by this InSAR time series. On larger time windows (say, 1980–2001), the temporal decorrelation between the viscoelastic model and the lake load would appear very clearly. Viscoelastic models with viscosities of 10^{17} Pa s and 10^{19} Pa s are discarded because the modeled ground motion amplitudes are too high and too low, respectively, compared to data (the model response for a viscosity of 10^{19} Pa s is mostly elastic in the period 1992–2001). Finally, we test the trade-off between the elastic thickness and the upper mantle viscosity. As expected, for a viscosity of 10^{18} Pa s, a lower elastic thickness (22 km) yields an increased model amplitude, whereas a larger elastic thickness (42 km) leads to a lowered modeled deformation (Figure 15b). To fit the data with a lower elastic thickness would require an underlying layer viscosity slightly above 10^{18} Pa s.

6.4. Spatial Comparison

[50] A stack of reconstructed interferograms ($\sum_{k-i}^{j-1} m_k$) between master dates, i, and slave dates, j, is computed to retrieve the spatial shape of the ground deformation representative of the whole data set. The stack, S_T, uses three reference images as master images, with little atmospheric delays after tropostatic corrections (20 January 1996, 5 January 1997, and 25 January 1998, or i_1, i_2, i_3, respectively). All images are used as slave images, excluding four images with a strong APS (first three and last one). The stack can then be written as a double sum over master and slave images of reconstructed interferograms:

$$S_T = \sum_{i=i_1,i_2,i_3} \sum_{j=4}^{M-1} \delta \left(\sum_{k=i}^{j-1} m_k \right) \tag{7}$$

where δ is equal to 1 or -1 depending on the sign the lake elevation difference between dates i and j. As averaging is efficient to remove the APS, we choose to stack reconstructed interferograms obtained after a moderate amount of smoothing ($r_m = r_l = 10$ yr^{-2}). This insures that no amplitude is lost by smoothing, and thus in the stack.

[51] The stack of reconstructed interferograms is compared with the stacks obtained with equation (7), but using modeled interferograms (Figure 16). Both the amplitude and spatial shape of the retrieved ground motion are well explained by the viscoelastic model (M2, $\eta = 10^{18}$ Pa s and $h = 32$ km) except for a few areas close to the lake as discussed above (Figure 16d). The spatial correlation coefficient between data and the viscoelastic model is high (0.88), slightly, but not significantly, larger than that between data and the elastic model (0.85). However, the elastic model amplitude is too small by a factor of 1.47, whereas the viscoelastic model amplitude agrees well with data. Profiles across the lake shown on Figure 17 emphasize the good agreement in shape between data and the viscoelastic model. If the elastic model amplitude is

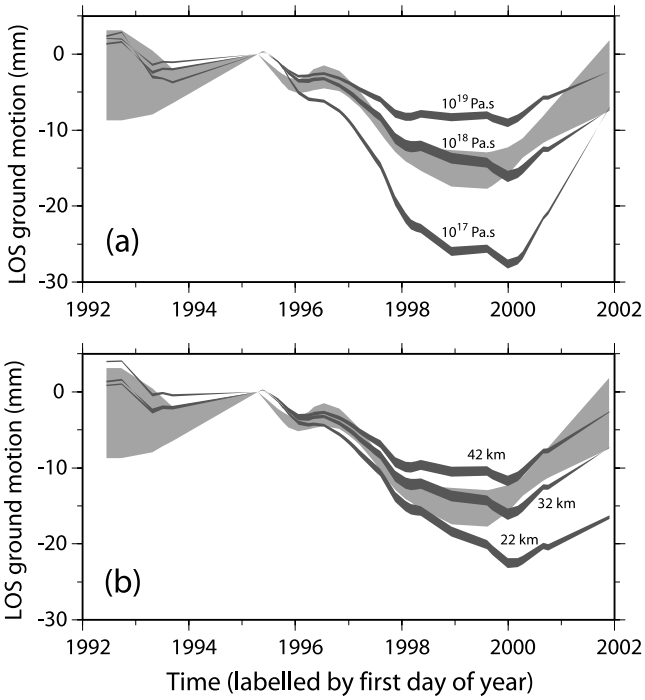

Figure 15. Comparison between retrieved ground motion (light grey area, see legend of Figure 14) and predicted motion from viscoelastic models (dark grey areas) (a) with varying incompetent layer viscosities (curve label) or (b) for a mantle viscosity of 10^{18} Pa s with varying elastic thicknesses (curve label). The dark grey areas include the models for the three locations shown in Figure 5d.

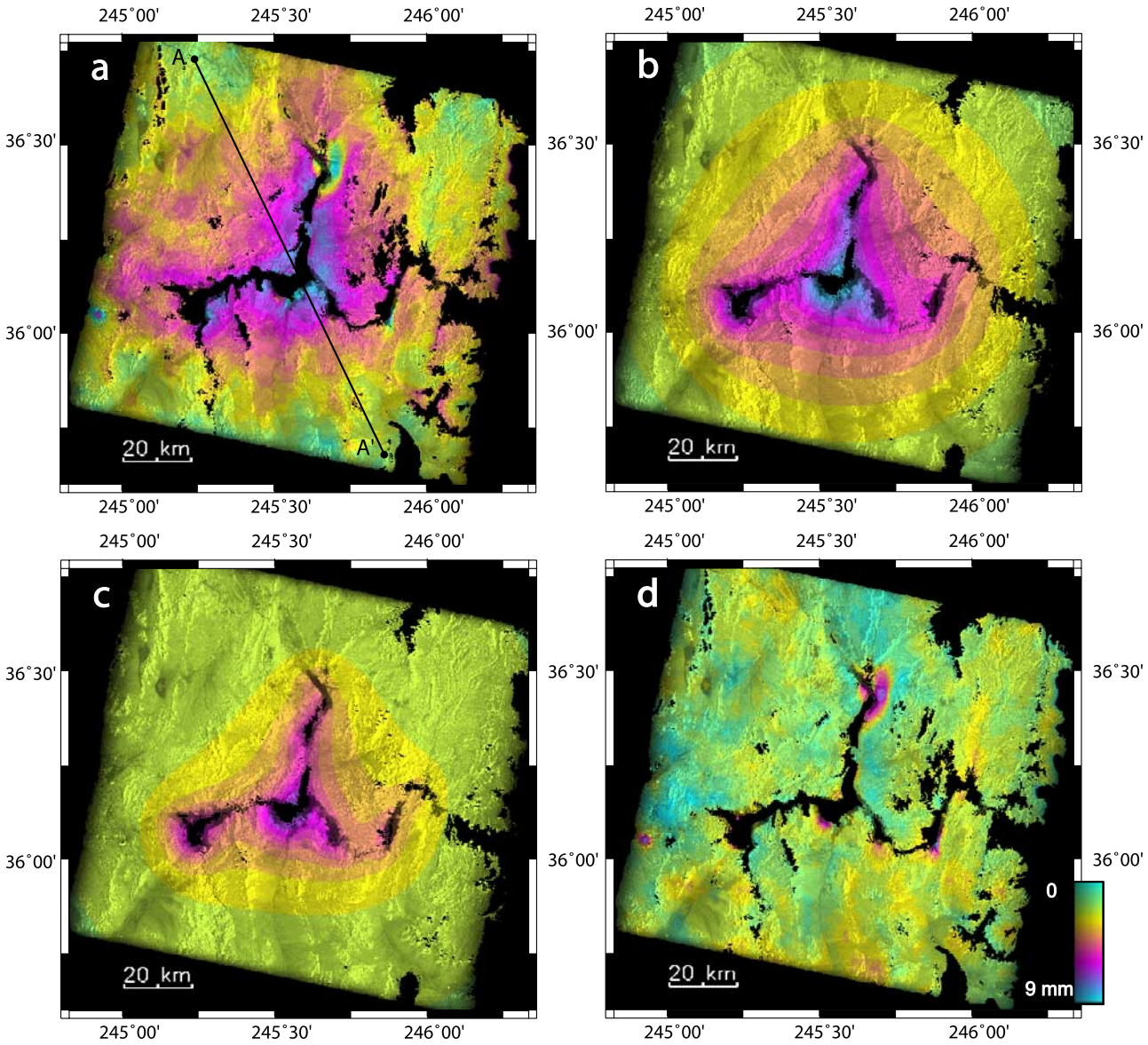

Figure 16. Comparison between (a) the stack of reconstructed interferograms obtained with a low level of data smoothing and the stacks of the predicted motion using (b) viscoelastic and (c) elastic model. The modeled ground motions in Figures 16b and 16c represent a stack of modeled displacements between the same dates as in (Figure 16a). (d) Corresponds to the residue, (Figures 16b and 16a), showing the poroelastic response of few areas close to the lake, and the motion due to the aquifer system deformation near Las Vegas.

multiplied by a factor 1.5, data and elastic model profiles also show a good agreement.

6.5. Elasticity Versus Poroelasticity

[52] The elastic model is discarded because it yields an underestimated amplitude. However, elastic models using elastic moduli lowered by a factor of 1.5 would successfully fit the data. This would imply to reduce V_p and V_s by 20%, yielding unrealistic low V_p velocities (less than 4.9 km s^{-1} for the average crust and less than 6.4 km s^{-1} for the upper mantle). One suggestion to decrease effective elastic moduli while maintaining realistic seismic velocities would be to take into account the difference between drained or undrained poroelastic behaviors. Seismic wave propagation mainly corresponds to an undrained elastic deformation. As the lake load is applied on a larger time scale than seismic waves, the relaxation of pore pressure heterogeneities by the upper crust draining could change the subsidence amplitude. Assuming that the upper crust is "instantaneously" (over less than a few months) drained, while the lower crust and mantle remain undrained, the deformation is computed by decreasing the Poisson ratio in the upper crust from 0.25 (undrained) to 0.21 (drained), while keeping the same shear modulus (Table 1, M3) [e.g., *Peltzer et al.*, 1996, 1998; *Freed et al.*, 2006]. These conditions of quick draining yield an "in phase" subsidence increase lower than 10%. Therefore explaining InSAR ground motion by a lowered effective poroelastic

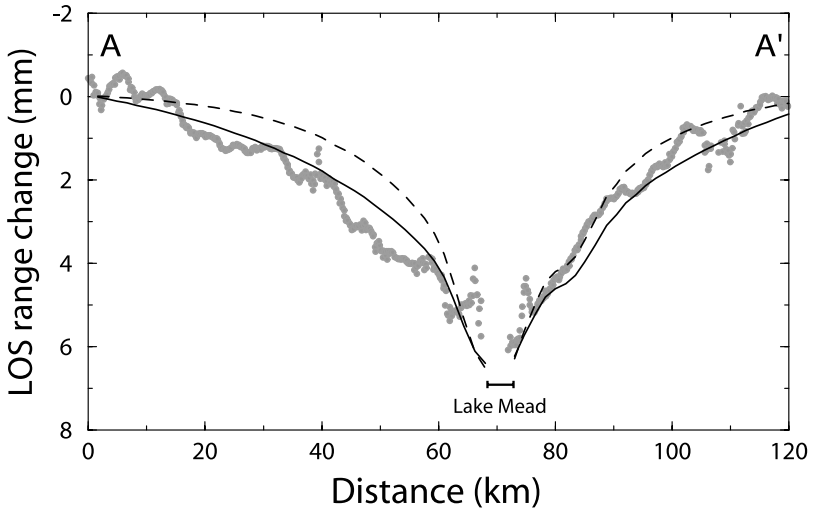

Figure 17. Comparison of the ground motion profile along A-A' (extracted from stacks on Figure 16), retrieved from InSAR analysis (solid grey circles), or computed with a viscoelastic model (solid black line), and an elastic model multiplied by a factor 1.5 (dashed black line).

modulus would required a very large Poisson ratio decrease over a very deep layer with rapid draining.

[53] Furthermore, this too simple approach excludes the counteracting effect of pore pressure diffusion away from the lake, due to pore pressure variations below the lake. At this stage of the analysis, we do not exclude that a poroelastic model could explain the deformation pattern observed in the lake Mead area, although important delayed effects should then be expected.

7. Conclusion

[54] We have computed 241 interferograms based on 43 SAR ERS images in order to analyze the temporal evolution of ground motion in the Lake Mead area. Although strong atmospheric delays mask the expected signal in most individual interferograms, a careful time series analysis enables to recover the ground motion associated with the lake level fluctuations. The methodology presented in this study allows to retrieve a small ground motion over a large area, without a priori constraints on the deformation behavior in time. A crucial step here is to choose both the data weighting and the smoothing level that maximize the signal-to-noise ratio in the retrieved ground motion. This ratio for the raw data is initially very low. The analysis of the coherent signal in time allows to discriminate between random APS and continuous deformation. We emphasize the importance of residual orbital fringes and tropostatic corrections for each interferogram before proceeding to the temporal analysis. The retrieved ground motion can be beyond doubts associated with the lithosphere response to the well documented lake load. Local deformation patterns associated with water table variations in sedimentary layers, are also mapped with accuracy, and differentiated from the regional motion.

[55] Elastic and viscoelastic forward models are performed to compare modeled and retrieved ground motion. A viscoelastic model using rheological parameters from *Kaufmann and Amelung* [2000] explains very well the data, whereas elastic models are discarded as they underestimate the ground motion amplitude. The mantle viscosity of 10^{18} Pa s, used in this model to adjust InSAR ground motion, agrees with previous estimates of upper mantle viscosity in the western United States, within the range of 10^{18}–10^{19} Pa s [*Dixon et al.*, 2004]. These viscosities are low compared to global estimates derived from postglacial studies. *Dixon et al.* [2004] suggest that this could be due to a high water content in the former mantle wedge inherited from the Farallon plate subduction.

[56] In this study, most data are acquired between 1995 and 2000 during a period of lake level increase. During this period, the predicted differences in temporal and spatial shapes between viscoelastic and elastic responses are small and thus difficult to detect. On a larger time period, the differences between elastic, poroelastic, and viscoelastic responses will increase. In the future, we expect InSAR data to be able to bring tight constraints on the lithosphere rheology.

Appendix A: Equations and Code Setup

[57] In the case of a flat Earth and for wavelength at which self-gravitation is negligible, the momentum equation writes as [*Cathles*, 1975]

$$\nabla \cdot \tau - \rho_0 g_0 \nabla u_z + \rho_0 g_0 (\nabla \cdot \mathbf{u}) \mathbf{e}_z = 0 \tag{A1}$$

where τ is the stress tensor deviation from the hydrostatic state, $\mathbf{u}$ is the displacement, $\rho_0 g_0$ is the product of density and gravity acceleration, and $\mathbf{e}_z$ is a vertical unit vector.

[58] In the case of a periodic load and deformation in time, the correspondence principle between elastic and Maxwell viscoelastic compressible media yields equivalent $\lambda^\star$ and $\mu^\star$ viscoelastic Lamé parameters:

$$\lambda^\star(\omega) = \frac{\lambda i\omega + \mu K/\eta}{i\omega + \mu/\eta} \tag{A2}$$

$$\mu^\star(\omega) = \frac{\mu i\omega}{i\omega + \mu/\eta} \tag{A3}$$

where λ, μ, K are the elastic Lamé parameters and compressibility, respectively, η is viscosity, and ω is the pulsation in time. The elastic parameters and viscosity depend only on depth. The model equations (A1) with a Maxwell rheology (A2)–(A3) are then linear. Therefore the medium response to a surface load can be computed as the sum of harmonic load responses, obtained by three-dimensional (3-D) Fourier transform in space (x, y) and time. Fourier decomposition on the horizontal plane (x, y) of any 2-D load pattern reduces to the sum of one dimensional sinusoids of the form $e^{i\mathbf{k}\cdot\mathbf{r}}$, where $\mathbf{k} = k_x\mathbf{e_x} + k_y\mathbf{e_y}$ is the wave number and $\mathbf{r} = x\mathbf{e_x} + y\mathbf{e_y}$. The equations in the directions parallel and perpendicular (along $\mathbf{k}$) to the sinusoid are then decoupled [*Cathles*, 1975]. Computing the individual response to a 1-D sinusoidal surface load can be achieved by writing stresses, τ, and displacements, $\mathbf{u}$, in the form

$$\tau_{zz} = \tilde{\tau}_{zz}(z)\exp(i\omega t)\exp(ikr) \tag{A4}$$

$$\tau_{rz} = \tilde{\tau}_{rz}(z)\exp(i\omega t)\exp(ikr) \tag{A5}$$

$$u_z = \tilde{u}_z(z)\exp(i\omega t)\exp(ikr) \tag{A6}$$

$$u_r = \tilde{u}_r(z)\exp(i\omega t)\exp(ikr) \tag{A7}$$

The space and temporal transformation of the equation of motion then leads to

$$\partial_z \begin{bmatrix} \tilde{u}_r \\ \tilde{u}_z \\ \tilde{\tau}_{rz} \\ \tilde{\tau}_{zz} \end{bmatrix} = \begin{bmatrix} 0 & -ik & \frac{1}{\mu^*} & 0 \\ -\frac{ik\lambda^*}{\lambda^*+2\mu^*} & 0 & 0 & \frac{1}{\lambda^*+\mu^*} \\ \frac{4k^2\mu^*(\lambda^*+\mu^*)}{\lambda^*+2\mu^*} & \rho_0 g_0 ik & 0 & -\frac{ik\lambda^*}{\lambda^*+2\mu^*} \\ -\rho_0 g_0 ik & 0 & -ik & 0 \end{bmatrix} \cdot \begin{bmatrix} \tilde{u}_r \\ \tilde{u}_z \\ \tilde{\tau}_{rz} \\ \tilde{\tau}_{zz} \end{bmatrix} \tag{A8}$$

[59] At the surface, we adopt a free slip boundary condition, $\tilde{\tau}_{rz} = 0$. To obtain the surface displacement kernels, the amplitude of the harmonic load at the surface is set to -1 ($\tilde{\tau}_{zz} = 1$). At the box bottom, we set $\tilde{\tau}_{zz} = \tilde{\tau}_{rz} = 0$. Note that here, because the applied harmonic surface load is periodic with a null average value, the average surface load is zero and equilibrium can be achieved with a bottom value for τ_{zz} uniformly equal to zero. The two points boundary value problem above (A8) is solved using IMSL routines. The kernels have been tested against a few analytical solutions [*Cathles*, 1975]. Finally, the coefficients of the 3-D Fourier load decomposition, for each wave number, k, and pulsation, ω, are multiplied by surface displacement kernels, except for the average uniform load which is not taken into account. Inverse 3-D (t, x, y) transformations then yield the modeled horizontal and vertical surface displacement fields, with zero average values. At each time step, the displacement fields are then referenced to the model corner (x = 0, y = 0), assumed motion less.

Notation

$\lvert$APS$\rvert$	APS amplitude for each SAR image.
$\mathbf{b}$	(N) vector with N perpendicular baselines.
$\mathbf{d}$	(N) data vector from N interferograms.
e_{DEM}	coefficient proportional to DEM error.
g	gravity acceleration (m s^{-2}).
$\mathbf{G}$	data kernel matrix.
h	layer thickness (km).
h_W	height scale of the humid atmosphere (m).
$\mathbf{m}$	(M-1) vector with displacement increments between M SAR images.
M	number of SAR scenes.
N	number of interferograms.
q_{ij}	interferogram "quality."
q_a	specific humidity (kg kg^{-1}).
$\overline{q_a}$	water vapor content (kg m^{-3}).
$r_m(\gamma)$	data roughness as a function of γ (yr^{-2}).
r_l	roughness of lake level fluctuations (yr^{-2}).
$\mathbf{s}$	(M) vector with phase/elevation slopes.
S	phase/elevation linear regression slope.
S_T	ground motion stack.
T_{2m}	temperature (K) at 2 m.
TCWV	total column of water vapor (kg m^{-2}).
$\mathbf{u}$	displacement.
$\mathbf{W}$	weighting matrix.
β	correlation coefficient.
γ	smoothing factor.
η	viscosity (Pa s).
λ	Lamé parameter (Pa).
μ	shear modulus (Pa).
ρ	density.
$\langle\, \sigma_m \,\rangle$	standard deviation of cumulative displacement.
τ	stress (Pa).
φ_{ij}	interferometric phase between image i and j.
φ_{RMS}	RMS between synthetic and original interferograms (mm).
ω	temporal weight of the smoothing operator.

[60] **Acknowledgments.** We would like to thank the European Space Agency (ESA) for supplying ERS images through a category 1 project. We are grateful to USGS for providing sediment thickness and bathymetric maps of Lake Mead and to ECMWF for the meteorological data. This manuscript benefited from discussions with Luce Fleitout and Rémy Roca. The reviews greatly improved the paper. This project has been funded by a grant from the ACI "Observation de la terre."

References

Amelung, F., D. L. Galloway, J. W. Bell, H. A. Zebker, and R. J. Laczniak (1999), Sensing the ups and downs of Las Vegas: InSAR reveals structural control of land subsidence and aquifer-system deformation, *Geology*, *27*, 483–486.

Berardino, P., G. Fornaro, R. Lanari, and E. Sansosti (2002), A new algorithm for surface deformation monitoring based on small baseline differential SAR interferograms, *IEEE Trans. Geosci. Remote Sens.*, *40*, 2375–2383.

Brady, R., B. Wernicke, M. McNutt, J. Mutter, and G. Correa (2000), Results of the Basin and Range Geoscientific Experiment (BARGE): A marine-style seismic reflection survey across the eastern boundary of the central Basin and Range Province, *Geochem. Geophys. Geosyst.*, *1*(9), doi:10.1029/2000GC000078.

Bürgmann, R., P. A. Rosen, and E. J. Fielding (2000), Synthetic aperture radar interferometry to measure Earth's surface topography and its deformation, *Annu. Rev. Earth. Planet. Sci.*, *28*, 169–209.

Cathles, L. M. (1975), *The Viscosity of the Earth's Mantle*, 386 pp., Princeton Univ. Press, Princeton, N. J.

Chaabane, F., A. Avallone, F. Tupin, P. Briole, and H. Maitre (2004), Correction of local and global tropospheric effects of differential SAR interferograms for the study of earthquake phenomena, *Eur. Space Agency Spec. Publ., ESA SP-550.*

Dixon, J. E., T. H. Dixon, D. R. Bell, and R. Malservisi (2004), Lateral variation in upper mantle viscosity: Role of water, *Earth. Planet. Sci. Lett.*, *222*, 451–467.

Duebendorfer, E. M., and E. T. Wallin (1991), Basin development and syntectonic sedimentation associated with kinematically coupled strike-slip and detachment faulting, southeastern Nevada, *Geology*, *19*, 87–90.

Farr, T. G., and M. Kobrick (2000), Shuttle radar topography mission produces a wealth of data, *Eos Trans. AGU*, *81*, 583–585.

Ferretti, A., C. Prati, and F. Rocca (2000), Nonlinear subsidence rate estimation using permanent scatterers in differential SAR interferometry, *IEEE Trans. Geosci. Remote Sens.*, *38*, 2002–2012.

Ferretti, A., C. Prati, and F. Rocca (2001), Permanent scatterers in SAR interferometry, *IEEE Trans. Geosci. Remote Sens.*, *39*, 8–20.

Feuerbach, D. L., E. I. Smith, J. D. Walker, and J. A. Tangemen (1993), The role of the mantle during crustal extension: Constraints from geochemistry of volcanic rocks in the Lake Mead area, Nevada and Arizona, *Geol. Soc. Am. Bull.*, *105*, 1561–1575.

Fleitout, L., Y. Krien, and G. Cailletaud (2005), Post-glacial rebound, lateral viscosity variations and transient creep, paper presented at 9th International Workshop on Numerical Modeling of Mantle Convection and Lithospheric Dynamics, Ettore Majorana Cent. for Sci. Cult., Erice, Italy.

Freed, A. M., R. Brgmann, E. Calais, J. Freymueller, and S. Hreinsdóttir (2006), Implications of deformation following the 2002 Denali, Alaska, earthquake for postseismic relaxation processes and lithopheric rheology, *J. Geophys. Res.*, *111*, B01401, doi:10.1029/2005JB003894.

Goldstein, R. M., and C. L. Werner (1998), Radar interferogram filtering for geophysical applications, *Geophys. Res. Lett.*, *25*, 2517–2520.

Gourmelen, N., and F. Amelung (2005), Postseismic mantle relaxation in the Central Nevada Seismic Belt, *Science*, *310*, 1473–1476.

Hanssen, R. F. (2001), *Radar Interferometry, Data Interpretation and Error Analysis*, 308 pp., Springer, New York.

Hetland, E. A., and B. H. Hager (2003), Postseismic relaxation across the Central Nevada Seismic Belt, *J. Geophys. Res.*, *108*(B8), 2394, doi:10.1029/2002JB002257.

Kaufmann, G., and F. Amelung (2000), Reservoir-induced deformation and continental rheology in the vicinity of Lake Mead, Nevada, *J. Geophys. Res.*, *105*, 16,381–16,358.

Lambeck, K., P. Johnston, C. Smither, and M. Nakada (1996), Glacial rebound of the British Isles—III. Constraints on mantle viscosity, *Geophys. J. Int.*, *125*, 340–354.

Lambeck, K., C. Smither, and P. Johnston (1998), Sea-level change, glacial rebound and mantle viscosity for northern Europe, *Geophys. J. Int.*, *134*, 102–144.

Lara, J. M., and J. I. Sanders (1970), The 1963–64 Lake Mead survey, technical report, Bur. of Reclam., U. S. Dep. of Inter., Washington, D. C.

Li, Z., J.-P. Muller, and P. Cross (2003), Comparaison of precitable water vapor derived from radiosonde, GPS and Moderate-Resolution Imaging Spectroradiometer measurements, *J. Geophys. Res.*, *108*(D20), 4651, doi:10.1029/2003JD003372.

Li, Z., J.-P. Muller, P. Cross, and E. J. Fielding (2005), Interferometric synthetic aperture radar (InSAR) atmospheric correction: GPS and Moderate Resolution Imaging Spectroradiometer (MODIS), and InSAR integration, *J. Geophys. Res.*, *110*, B03410, 4651, doi:10.1029/2004JB003446.

Longwell, C. R. (1960), Interpretation of the levelling data, in *Comprehensive Survey of Sedimentation in Lake Mead, 1948–49*, edited by W. O. Smith, C. P. Vetter, and C. B. Cummings, *U. S. Geol. Surv. Prof. Pap.*, *295*, 33–38.

Menke, W. (1989), *Geophysical Data Analysis: Discrete Inverse Theory*, 289 pp., Elsevier, New York.

Nakiboglu, S. M., and K. Lambeck (1983), A reevaluation of the isostatic rebound of Lake Bonneville, *J. Geophys. Res.*, *88*, 10,439–10,447.

Nishimura, T., and W. Thatcher (2003), Rheology of the lithosphere inferred from postseismic uplift following the 1959 Hebgen Lake earthquake, *J. Geophys. Res.*, *108*(B8), 2389, doi:10.1029/2002JB002191.

Peltier, W. R. (1984), The thickness of the continental lithosphere, *J. Geophys. Res.*, *89*, 11,303–11,316.

Peltzer, G., P. Rosen, F. Rogez, and K. Hudnut (1996), Postseismic rebound in fault step-overs caused by pore fluid flow, *Science*, *273*, 1202–1204.

Peltzer, G., P. Rosen, F. Rogez, and K. Hudnut (1998), Poroelastic rebound along the Landers 1992 earthquake surface rupture, *J. Geophys. Res.*, *103*, 30,131–30,145.

Peltzer, G., F. Crampé, S. Hensley, and P. Rosen (2001), Transient strain accumulation and fault interaction in the Eastern California shear zone, *Geology*, *29*, 975–978.

Pollitz, F., G. Peltzer, and R. Burgmann (2000), Mobility of continental mantle: Evidence from postseismic geodetic observations following the 1992 Landers earthquake, *J. Geophys. Res.*, *105*, 8035–8054.

Priestley, K., J. A. Orcutt, and J. N. Brune (1980), Higher-mode surface waves and structure of the Great Basin of Nevada and western Utah, *J. Geophys. Res.*, *85*, 7166–7174.

Roller, J. C., and J. H. Healy (1963), Seismic-refraction measurements of crustal structure between Santa Monica Bay and Lake Mead, *J. Geophys. Res.*, *68*, 5837–5849.

Rosen, P. A., S. Hensley, I. R. Joughin, F. K. Lin, S. N. Madsen, R. Rodriguez, and R. M. Goldstein (2000), Synthetic aperture radar interferometry—Invited paper, *Proc. IEEE*, *88*, 333–382.

Rosen, P. A., S. Hensley, G. Peltzer, and M. Simons (2004), Updated repeat orbit interferometry package released, *Eos Trans. AGU*, *85*(5), 47.

Scharroo, R., and P. N. A. M. Visser (1998), Precise orbit determination and gravity field improvement for the ERS satellites, *J. Geophys. Res.*, *103*, 8113–8127.

Schmidt, D. A., and R. Bürgmann (2003), Time-dependent land uplift and subsidence in the Santa Clara valley, California, from a large interferometric synthetic aperture radar data set, *J. Geophys. Res.*, *108*(B9), 2416, doi:10.1029/2002JB002267.

Twichell, D. C., V. A. Cross, M. Rudin, and K. Parolski (1999), Surficial geology and distribution of post-impoundment sediment of the western part of Lake Mead based on a sidescan sonar and high-resolution seismic-reflection survey1, *U. S. Geol. Surv. Open File Rep., OF99-581*.

Twichell, D. C., V. A. Cross, and S. D. Belew (2003), Mapping the floor of Lake Mead (Nevada and Arizona): Preliminary discussion and GIS data release, *U. S. Geol. Surv. Open File Rep., OF03-320*.

Uppala, S., P. Kållberg, A. Simmons, and U. Andrae (2005), The ERA-40 re-analysis, *Q. J. R. Meteorol. Soc.*, *131*, 2961–3012.

Webley, P. W., R. M. Bingley, A. H. Dodson, G. Wadge, S. J. Waugh, and I. N. James (2004), Atmospheric water vapour correction to InSAR surface motion measurements on mountains: Results from a dense GPS network on Mount Etna, *Phys. Chem. Earth*, *27*, 363–370.

Wernicke, B., and G. J. Axen (1988), On the role of isostasy in the evolution of normal fault systems, *Geology*, *16*, 848–861.

Wernicke, B., G. J. Axen, and J. K. Snow (1988), Basin and Range extensional tectonics at the latitude of Las Vegas, Nevada, *Geol. Soc. Am. Bull.*, *100*, 1738–1757.

Wernicke, B., J. L. Davis, R. A. Bennett, J. E. Normandeau, A. M. Friedrich, and N. A. Niemi (2004), Tectonic implications of a dense continuous GPS velocity field at Yucca Mountain, Nevada, *J. Geophys. Res.*, *109*, B12404, doi:10.1029/2003JB002832.

Wright, T., B. Parsons, and E. Fielding (2001), Measurement of interseismic strain accumulation across the North Anatolian Fault by satellite radar interferometry, *Geophys. Res. Lett.*, *28*, 2117–2120.

Zandt, G., S. C. Myers, and T. C. Wallace (1995), Crust and mantle structure across the Basin and Range–Colorado Plateau boundary at 37°N latitude and implications for Cenozoic extensional mechanism, *J. Geophys. Res.*, *100*, 10,529–10,548.

Zebker, H. A., P. A. Rosen, and S. Hensley (1997), Atmospheric effects in interferometric synthetic aperture radar surface deformation and topographic maps, *J. Geophys. Res.*, *102*, 7547–7563.

P. Briole, Institut de Physique du Globe de Paris, CNRS, 4 Place Jussieu, F-75005 Paris, France.

O. Cavalié, M.-P. Doin, and C. Lasserre, Laboratoire de Géologie, École Normale Supérieure, CNRS, 24 rue Lhomond, F-75231 Paris cedex 05, France. (cavalie@geologie.ens.fr)